Probing how Ti- and Nb-substitution affect the stability and improve the electrochemical performance of β- and ε-LiVOPO₄

Journal:	*Journal of Materials Chemistry A*
Manuscript ID	TA-ART-10-2022-008184.R1
Article Type:	Paper
Date Submitted by the Author:	24-Dec-2022
Complete List of Authors:	Hidalgo, Marc; Binghamton University, Materials Science and Engineering Buyuker, Isiksu; Binghamton University, Materials Science and Engineering Kamm, Gabrielle; Stony Brook University, Department of Chemistry Zhu, Zhuoying; UCSD, Grenier, Antonin; X-ray Science Division, Advanced Photon Source, Argonne National Laboratory Zuba, Mateusz; Binghamton University, Physics, Applied Physics and Astronomy Deng, Zhi; University of California, San Diego, Department of NanoEngineering Zong, Yanxu; Binghamton University, Materials Science and Engineering Kaplan, Carol; Binghamton University, Chemistry Chernova, Natasha; Binghamton University, Zhou, Guangwen; Binghamton University, Mechanical Engineering Piper, Louis; Binghamton University, State University of New York, Department of Physics, Applied Physics, and Astronomy Ong, Shyue Ping; University of California, San Diego, Nanoengineering Chapman, Karena; Stony Brook University, Chemistry Whittingham, Stanley; SUNY Binghamton

SCHOLARONE™
Manuscripts

ARTICLE

Probing how Ti- and Nb-substitution affect the stability and improve the electrochemical performance of β- and ε-LiVOPO$_4$

Marc Francis V. Hidalgo,[a$] Isik Su Buyuker,[a$] Gabrielle E. Kamm,[b] Zhuoying Zhu,[c] Antonin Grenier,[b] Mateusz J. Zuba,[a] Zhi Deng,[c] Yanxu Zong,[d] Carol Kaplan,[a] Natasha A. Chernova,[a] Guangwen Zhou,[d] Louis F. J. Piper,[a] Shyue Ping Ong,[c] Karena W. Chapman,[b] M. S. Whittingham[a]

LiVOPO$_4$ is a promising next-generation multi-electron cathode material, boasting a theoretical capacity of 305 mAh/g, significantly higher than any commercially used Li-ion battery cathode material. However, the material still faces several limitations, including the difficulty in attaining the full theoretical capacity at higher rates and capacity fade over several cycles. In this paper, we show that Ti- and Nb-substitution can be used to improve the thermal stability and electrochemical performance of LiVOPO$_4$. We show through in-situ heating with XRD and a novel gradient heating technique that both Ti- and Nb-substitution cause β-LiVOPO$_4$ to be stabilized relative to ε-LiVOPO$_4$. This is due to transition-metal substitution, which increases the O-vacancy formation energies, pushing the β → ε transition to higher temperatures. We show that it is still possible to synthesize pure-phase ε-LiVOPO$_4$ through the use of high temperatures to generate these O-vacancies. We show that even 1% of Ti- or Nb-substitution can improve the initial capacity and long term cycling capability of LiVOPO$_4$ by improving the high-voltage capacity and reducing the capacity fade in both the high- and low-voltage regions. This is due to the an overall improved Li$^+$ ion diffusion which is caused by an improved charge-transfer resistance during cycling.

Introduction

Li-ion batteries are currently the most ubiquitous form of energy storage for portable electronic devices due to their high energy density.[1-4] However, with the rise of more powerful devices, including electric vehicles, the demand for more energy-dense Li-ion batteries is increasing.[5-7] In order to improve the energy density, either the mass of the non-active elements in the cathode must decrease or multiple Li$^+$ ions must be intercalated per gram of material.[8-13] One promising cathode material utilizing the latter method is lithium vanadyl phosphate (LiVOPO$_4$).[14-16] The vanadium has two redox couples within the voltage window of the electrolyte: V^{5+}/V^{4+} and V^{4+}/V^{3+} at 4.0 V and 2.5 V, respectively. This allows LiVOPO$_4$ to intercalate up to two Li$^+$ ions, going through the transition of VOPO$_4$ ↔ LiVOPO$_4$ ↔ Li$_2$VOPO$_4$, resulting in a theoretical capacity of 305 mAh/g and a specific energy of over 900 Wh/kg.[17-19] Although LiVOPO$_4$ has three major polymorphs (α$_I$, β, and ε), we have shown previously that the β and ε polymorphs are the more promising polymorphs due to their superior thermal stability, capacity, and long-term cycling performance.[20, 21]

Although thermodynamically similar,[20-22] the β-LiVOPO$_4$ polymorph has an orthorhombic structure (Pnma) with 1D diffusion channels[23-25] while the ε-LiVOPO$_4$ polymorph has a triclinic structure (P$\bar{1}$) with pseudo-1D diffusion channels.[16, 22, 23, 26, 27] Additionally, the polymorphs differ in the amount of O-vacancies present, with ε-LiVOPO$_4$ being stabilized in the presence of O-vacancies.[20] Thus, β-LiVOPO$_4$ can transform into ε-LiVOPO$_4$ through the generation of O-vacancies within the structure. Conversely, the opposite transition is also possible, albeit at a slower rate, if the O-vacancies are filled.[20, 28]

Even when synthesized through different methods, most studies on LiVOPO$_4$ have difficulties in attaining theoretical capacity at higher rates. General methods to improve the capacity in Li-ion batteries include particle size reduction,[17, 29] improvements to crystallinity,[17, 30, 31] and the use of coatings.[29,32-34] Shi et al. showed that utilizing these techniques significantly improves the electrochemical performance of LiVOPO$_4$, approaching theoretical capacity, even at high C-rates. Siu et al. furthered this by showing full 2 Li cycling in nanosized and highly crystalline ε-VOPO$_4$ using graphene as a conducting additive. However, capacity quickly fades when cycling at higher C-rates. Thus, we propose the use of another technique to improve the electrochemical performance of LiVOPO$_4$: transition metal substitution.[32-38]

Although there have been several reports on transition-metal substitution into (Li)VOPO$_4$,[38-41] they all focus on intercalating only a single Li$^+$ ion, with the exception of Wen et al., who showed multi-Li cycling in Mo-substituted ε-VOPO$_4$.[38]

$Equal contribution
[a]NECCES, Binghamton University, Binghamton, NY 13902, USA. Email: stanwhit@gmail.com
[b]Department of Chemistry, Stony Brook University, NY 11794, USA. Email: karena.chapman@stonybrook.edu
[c]Department of NanoEngineering, University of California San Diego, 9500 Gilman Drive #0448, La Jolla, CA 92093, USA. Email: ongsp@eng.ucsd.edu
[d]Materials Science and Engineering Program & Department of Mechanical Engineering, State University of New York, Binghamton, New York 13902, USA Email: gzhou@binghamton.edu .

Additionally, all these studies focus solely on improving either β- or ε-LiVOPO$_4$, but not both. In this study, we propose utilizing Ti and Nb as our substituents, and characterizing its effects on multi-lithium intercalation in both β- and ε-LiVOPO$_4$. Ti is selected as a substituent due to LiTiOPO$_4$ having polymorphs with similar structures to both the β (orthorhombic)[42] and ε (triclinic)[43] polymorphs, with the orthorhombic structure being the more common form. Both have also been extensively studied for use in anodes, with a redox potential of ~1.5 V. Ti-substitution has also previously been employed in NMC's, where it has been shown to improve the capacity retention (even at levels of ~1%) by reducing the volume changes that occur during cycling, which then reduces cracking of the NMC particles.[44, 45] However, since Ti has a similar size to V, we do not expect this mechanism to be present in the Ti-substituted LiVOPO$_4$. A separate study has also reported the use of Ti-substitution into LiVOPO$_4$.[40] However, the study only focused on ε-LiVOPO$_4$ and did not take into consideration the effects of the large β-LiVOPO$_4$ impurity present nor the insertion of the second Li$^+$ ion to its electrochemical performance.

The other substituent selected, Nb, is from the same family as V. Both transition metals have similar bonding characteristics, theoretically making it likely that substitution would be successful. Nb has also been substituted in other cathode systems,[46-48] with a recent increased interest in its use as a substituent in (Li)VOPO$_4$.[49-51]

Overall, we predict Ti and Nb to have a high probability of successful substitution into LiVOPO$_4$. However, due to differences in atomic size and bonding characteristics, substitution will also have an effect on the thermodynamic stability of the host material used. Thus, in this study, we propose to study the effects of Ti and Nb substitution on both the thermodynamic stability and electrochemical performance of β- and ε-LiVOPO$_4$. We will be using the hydrated LiVOPO$_4$ precursor, LiVOPO$_4$·2H$_2$O, because we have shown that it is a useful precursor in studying the thermodynamic and electrochemical properties of both β- and ε-LiVOPO$_4$.[20, 21]

Methodology

Synthesis of substituted LiVOPO$_4$·2H$_2$O, β-LiVOPO$_4$, and ε-LiVOPO$_4$

LiVOPO$_4$·2H$_2$O was synthesized using the hydrothermal method with some modifications.[20, 27] V$_2$O$_5$ (Aldrich, >99.6%), oxalic acid (Sigma-Aldrich, >99.0%), and phosphoric acid (Fisher Scientific, 85%) were first dissolved in water and ethanol. If the samples were to be substituted, the amount of V$_2$O$_5$ was reduced and an equivalent molar amount of either (NH$_4$)$_2$(C$_2$O$_4$)$_2$TiO·H$_2$O (Fisher, 98%) or NH$_4$(C$_2$O$_4$)$_2$NbO·5H$_2$O (Sigma-Aldrich, 99.99%) was added. The solution was then stirred for 18 hours. Afterward, LiOH·H$_2$O (Sigma, >99.0%) was added, and stirred for another 4 hours. The solution was hydrothermally synthesized in a 4748 Type 125 mL PTFE-lined reactor (Parr Instrument Co.) and heated to 160 °C for 48 hours. The product was filtered, washed with water, ethanol, and acetone, then dried overnight at 60 °C. β-LiVOPO$_4$ was synthesized by heating the LiVOPO$_4$·2H$_2$O at 600 °C in O$_2$ for 3

hours, while ε-LiVOPO$_4$ was formed by annealing the same precursor at 900 °C in Ar for 3 hours.

Materials characterization

Powder X-ray diffraction (XRD) data was collected using a Bruker D8 Advance diffractometer utilizing a Cu Kα source (Kα1 = 1.54053 Å, Kα2 = 1.54431 Å) over the 2θ range of 10 ° – 80 ° and a step size of 0.02 °. Indexing, phase identification, and Rietveld refinement were conducted using the TOPAS software package (Bruker AXS, version 5.0) and the PDF-2016 software package. Phase quantification for the alumina was not included in the calculated total phase quantification data of LiVOPO$_4$ for the refinement of the data from the gradient heater. This is because alumina was used simply as a matrix material to hold the LiVOPO$_4$ in place during heating and analysis.

Thermogravimetric analysis (TGA) was performed using a TG 209 F1 Iris (260-TG) instrument at a ramp rate of 5 °C/min in Ar. Data was analyzed using Proteus.

Samples were prepared for analysis using inductively coupled plasma optical emission spectrometry (ICP) by first dissolving ~5 mg of LiVOPO$_4$ in aqua regia. If the sample contains Nb, then oxalic acid was also added. After dissolving, the solution was then diluted to 25 mL. The samples were analyzed using a Varian Vista-MPX Axial ICP-OES instrument.

High-resolution transmission electron microscopy (HRTEM) imaging was carried out on JEOL JEM 2100F operated at 200 kV.

In situ synchrotron XRD data were collected using high-energy x-rays (λ = 0.2410 Å) provided by beamline 17-BM at the Advanced Photon Source, Argonne National Laboratory. Diffraction images were recorded in transmission geometry using an area detector, and integrated with GSAS-II[52] using a LaB$_6$ standard (NIST SRM 660b) as a reference. LiVOPO$_4$·2H$_2$O (or transition-metal substituted analogues) were loaded in 1.1 mm diameter amorphous SiO$_2$ capillary tubes (F&D Glass) and heated under a controlled atmosphere (He or O$_2$, 20 cc/min) using the flow-cell furnace.[53]

For gradient heating, the heating elements of the flow-cell furnace were replaced by a 3D printed ceramic bar wound with Kanthal wire at an increasing pitch.[54] The material was mixed with alumina fiber to minimize movement of the sample powder within the capillary/thermal gradient following a change in volume associated with water loss at high temperatures. The samples were heated for 10 minutes and then cooled at 1 °C·s^{-1} to room temperature before collecting diffraction data at room temperature. The temperature along the gradient was estimated based on the observed offset between the lattice parameters and known coefficients of thermal expansion obtained for a mixture of α-Al$_2$O$_3$ and Si.[55] Lattice parameters were determined using LeBail refinement with the TOPAS software. Coefficients of thermal expansion were taken from literature.[56, 57] The temperature range determined from this method was 276-744˚C.

X-ray absorption spectroscopy (XAS) measurements were carried out using the synchrotron facilities of the National Synchrotron Light Source (NSLS-II). Ex-situ samples were measured at beamline 6BMM. V K-edge measurements were carried out in the transmission mode using the Si(111) double

ARTICLE

crystal mono-chromator and an unfocussed incident beam. XANES measurements of low concentration substituted elements were carried out in fluorescence mode using a fluorescence detector.

Electrochemical characterization

The particle size of β- and ε-LiVOPO$_4$ were first reduced prior to being turned into electrodes. This was done via high-energy ball-milling the powders with graphene for 30 minutes. The mixture was then combined with polyvinylidene fluoride (PVDF), resulting in a ratio of LiVOPO$_4$:graphene:PVDF of 75:15:10. A slurry was formed using n-methyl-2-pyrrolidinone (NMP) as the solvent, cast onto a carbon-coated Al foil, and dried at 60 °C. Electrodes were then punched out with a surface area of 1.2 cm^2 and active mass loadings ranging from 4.5 - 6.5 mg. The electrodes were then used as cathodes in 2325-type coin cells, with a Li chip (MTI) as the anode, a Celgard 2400 separator (Hoechst Celanese) as the separator, and 1 M LiPF$_6$ in 1:1 v/v ethylene carbonate (EC) and dimethyl carbonate (DMC) as the electrolyte. Electrochemical tests were conducted using a VMP multichannel potentiostat (Bio-Logic).

Charge-discharge tests were conducted at a rate of C/20 (C = 305 mAh/g) from 1.5 V to 4.5 V. Rate tests were conducted within the same voltage window at C-rates of C/40, C/20, C/10, and C/5. Cyclic voltammetry (CV) measurements were taken at scan rates of 0.05, 0.1, 0.2, and 0.4 mV/s. Overall Li$^+$ ion diffusion coefficients (D$_{CV}$) were estimated using the Randles-Sevick equation, with an area of 1.2 cm^2, Li$^+$ concentration of 0.019757 mol/cm^3, and electrons transferred of 1. This calculation of D$_{CV}$ for LiVOPO$_4$ is described in detail elsewhere.[21] Electrochemical impedance spectroscopy (EIS) measurements were conducted using the Potentio Electrochemical Impedance Spectroscopy method. The frequency range was from 200 kHz to 5 mHz, with 6 points taken per decade. The applied voltage oscillated between ±10 mV. EIS measurements were taken in triplicate to confirm that the system reached a steady state. A modified Randles circuit is used to model the measured EIS data and calculate the series (R$_s$) and charge-transfer (R$_{ct}$) resistances. The method for calculating the bulk Li$^+$ diffusion coefficient (D$_W$) is discussed in the supplementary section and is based on the method described by Ho et al.[58]

Computational methods

The pre-relaxed structures for β- and ε-LiVOPO$_4$ were obtained from the Materials Project[59] database with material IDs mp-26963 and mp-26091, respectively. For partially substituted structures, we considered all symmetrically distinct sites for 3.125%, 6.25%, 9.375% of Ti/Nb substitutions in a 2x2x2 supercell. When it comes to a higher substitution ratio of 12.5%, we used relatively smaller supercells (2x2x1, 2x1x2 and 1x2x2) to generate a reasonable number of orderings for structural relaxations (>500 if still using 2x2x2 supercell). After computing all enumerated structures, the lowest-energy configuration was then selected and used for the following calculations. Note that the diverse choice of substituted sites does have effect on stability: more dopants introduced, more diverse the substitution sites are, more thermodynamically

different the substituted structures will be. All density functional theory (DFT) calculations were performed using the Vienna Ab initio Simulation Package (VASP),[60] within the projector augmented wave approach.[61] The total energies of all partially substituted structures were calculated using the Perdew-Burke-Ernzerhof (PBE) generalized-gradient approximation (GGA)[62] functional with a Hubbard U[63] of 3.25 eV for vanadium, similar to that used in the Materials Project. All calculations were spin-polarized, with a plane wave energy cut-off of 520 eV and a k-point density of at least 1000/(number of atoms in the unit cell) applied. For phase stability assessment, all other pre-computed phases in the chemical systems of interest were obtained from the Materials Project database.[64]

To estimate the dopability of β- and ε-LiVOPO$_4$, we calculated the neutral dopant formation energy using the formalism by Wei et al.[65]

$$E_f[M] = E_{tot}[doped] - E_{tot}[bulk] - \sum_i n_i \mu_i$$

where $E_{tot}[doped]$ and $E_{tot}[bulk]$ are the total energies of the structure with and without the neutral dopant M, respectively. μ_i is the atomic chemical potential of species *i* that varies based on different experimental conditions; n_i is the number of atoms of species *i* being added ($n_i > 0$) or removed ($n_i < 0$) from the pristine structure. The lower bounds of the dopant formation energies are given in **Error! Reference source not found.**.

To investigate the β-to-ε transition in Ti/Nb-doped LiVOPO$_4$, we calculated the defect formation energies of O-vacancy using the following equation:

$$E_f[O_{vac}] = E_{tot}[Li_{32}V_{32-x}M_xP_{32}O_{159}] - E_{tot}[Li_{32}V_{32-x}M_xP_{32}O_{160}] + \mu_O$$

where $\Delta\mu_O = \mu_O - \frac{1}{2}\mu_{O_2}^0$ is the oxygen chemical potential relative to $\mu_{O_2}^0$, the reference state of O$_2$ gas at standard temperature and pressure. The oxygen vacancy was created in a 2x2x2 supercell at a concentration of 0.625%. The structure was relaxed until the energy and forces are converged to 10^{-5} eV and 0.05 eVÅ^{-1}, respectively.

The Helmholtz free energy was calculated using VASP's implementation of density functional perturbation theory (DFPT) and the Phonopy code.[66] 12.5% Nb- and Ti-doped LiVOPO$_4$ in 2x2x1 supercells with/without 1.25% oxygen
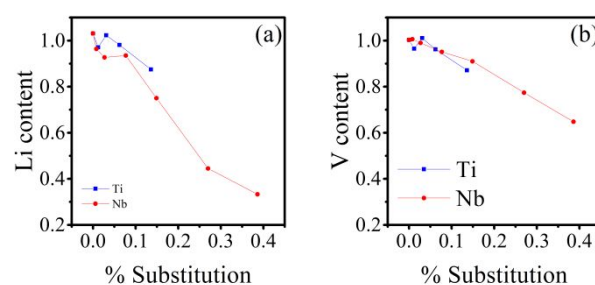

Fig. 1. ICP data showing changes in (a) Li and (b) V content relative to P (P = 1) calculated from ICP as transition-metal content increases.
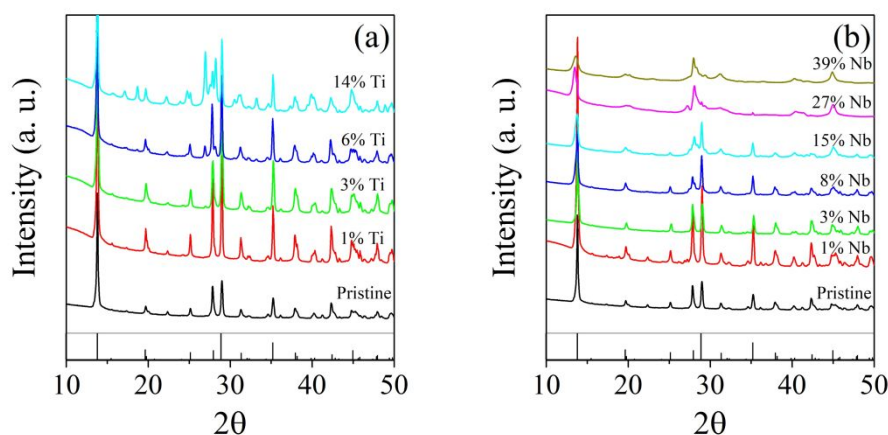
Fig. 2. XRD of (a) Ti- and (b) Nb-substituted $LiVOPO_4 \cdot 2H_2O$ (λ=1.54053 Å).

vacancy were used and a more strict energy convergence criterion of 10^{-8} eV was used for all DFPT calculations.

Results

Confirmation of substitution in $LiVOPO_4 \cdot 2H_2O$

$LiVOPO_4 \cdot 2H_2O$ synthesized using the hydrothermal method is used as the precursor for later forming $LiVOPO_4$. Substituted versions are synthesized by replacing appropriate amounts of V with the required amount of substituent during the synthesis. Inductively coupled plasma with optical emission spectrometry (ICP) is used to quantify the amounts of each element present in the $LiVOPO_4 \cdot 2H_2O$ (**Error! Reference source not found.**) and are plotted as the Li and V content vs % substitution (Fig. 1) to better show changes induced by substitution. The analysis shows that we are successful in introducing a controlled amount of substituent while simultaneously reducing the amount of V present. We also observe that Li-deficiencies are induced upon the introduction of the substituents. V-deficiencies are expected, as the transition-metals are substituting the V. Li-deficiencies are also expected in the Nb-substituted samples, as

V^{4+} is being replaced with Nb^{5+}. Our other studies have also shown that transition-metal substitution often exacerbates the introduction of protons within the hydrothermally synthesized $LiVOPO_4$ structure, which also leads to Li-deficiencies. This may also be the case for transition-metal substituted $LiVOPO_4 \cdot 2H_2O$, and may explain the presence of Li-vacancies in the Ti-substituted samples, even if V^{4+} is replaced with Ti^{4+}.

Powder X-ray diffraction (XRD) shows that the Ti-substituted $LiVOPO_4 \cdot 2H_2O$ remains pure-phase up to ~3% substitution (Fig. 2). Past 3% Ti-substitution, some amount of β-$LiVOPO_4$ forms, with the 6% and 14% Ti-substituted samples containing ~15% and ~55% β-$LiVOPO_4$, respectively. The formation of a separate β-$LiVOPO_4$ phase in the samples with higher amounts of Ti-substitution is expected because the orthorhombic $LiTiOPO_4$ has a structure similar to β-$LiVOPO_4$. The orthorhombic $LiTiOPO_4$ structure is also more stable than the triclinic $LiTiOPO_4$ structure,[67, 68] which explains why the orthorhombic phase forms instead of the triclinic one. We know that these side products are β-$LiVOPO_4$ and not $LiTiOPO_4$, since the amounts of this orthorhombic phase present are significantly larger than the amount of Ti in the sample. Since β-$LiVOPO_4$ is significantly more stable than $LiVOPO_4 \cdot 2H_2O$, it is not
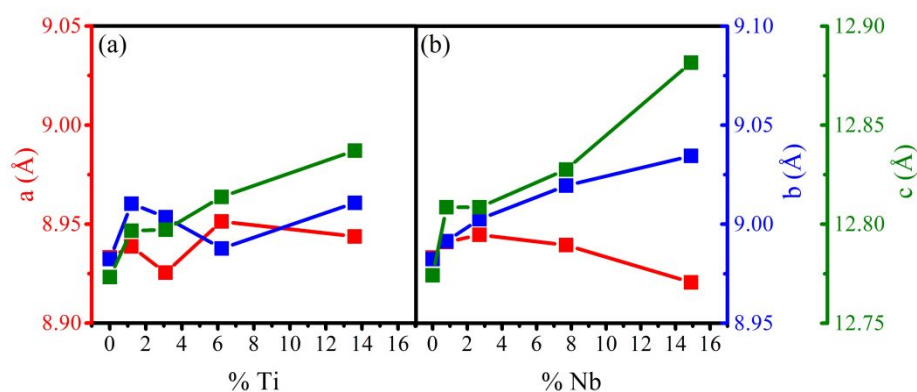

Fig. 3. Lattice parameters of (a) Ti- and (b) Nb-substituted $LiVOPO_4 \cdot 2H_2O$ showing successful transition-metal substitution into $LiVOPO_4 \cdot 2H_2O$.

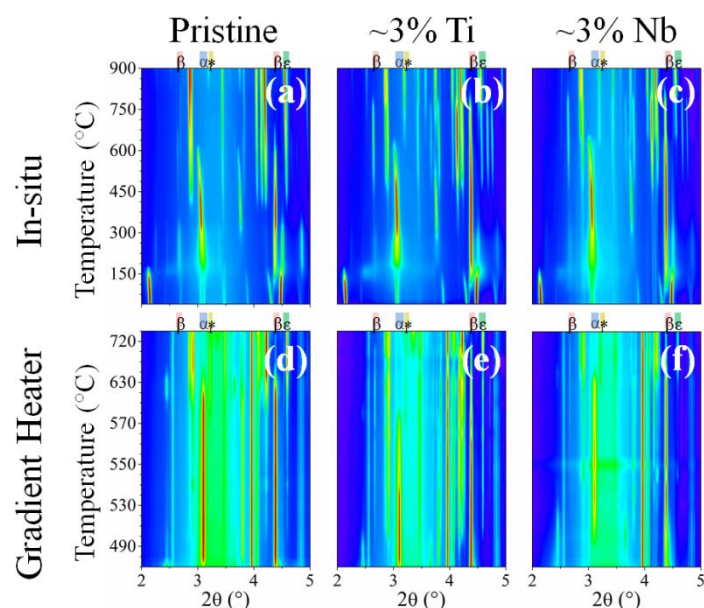Fig. 4. Comparison of XRD patterns of pristine and substituted LiVOPO$_4$·2H$_2$O in He via (a-c) the in-situ method and (d-f) the gradient heater method (λ = 0.2410 Å).

surprising that Ti-substitution into LiVOPO$_4$ would cause it to transform into β-LiVOPO$_4$ over LiVOPO$_4$·2H$_2$O. Since the goal of this study is to synthesize LiVOPO$_4$, these β-LiVOPO$_4$ side products are not considered as impurities.

On the other hand, the Nb-substituted samples steadily become more amorphous as the amount of Nb increases. Since there have been no reports on a LiNbOPO$_4$ crystal with the same structure as LiVOPO$_4$, we do not expect any polymorph of LiVOPO$_4$ to form as a side product in the same way as the Ti-substituted LiVOPO$_4$·2H$_2$O samples. In fact, we expect the Nb-substituted LiVOPO$_4$·2H$_2$O to remain with this layered structure since there have been reports of NbOPO$_4$·3H$_2$O,[69] which also has a layered structure.

If substitution is successful, we expect the lattice parameters to change following Vegard's law.[70] That is, since Ti and Nb are larger than V, we expect some or all of the lattice parameters to increase (Fig. 3). In the Ti-substituted LiVOPO$_4$·2H$_2$O, we observe that the b and c lattice parameters

increase with an increase in the amount of Ti, while the a lattice parameter only goes through relatively very smaller changes.

Similarly, the lattice parameters of the Nb-substituted LiVOPO$_4$·2H$_2$O increase consistently with substitution, with the c lattice parameter increasing the most, followed by the b lattice parameter. Although the *a* lattice parameter does increase slightly, it also tapers off after ~3% substitution and even decreases afterwards. These changes continue up to ~15% substitution. Further increasing the Nb-content results in very amorphous XRD patterns, meaning calculations of the lattice parameters above 15% Nb would be fairly dubious. Finally, note that the lattice parameter changes of the Nb-substituted LiVOPO$_4$·2H$_2$O are larger than that of the Ti-substituted samples since Nb is a much larger atom than Ti.

Overall, these show that substitution is successful for both Ti- and Nb-substituted LiVOPO$_4$·2H$_2$O.

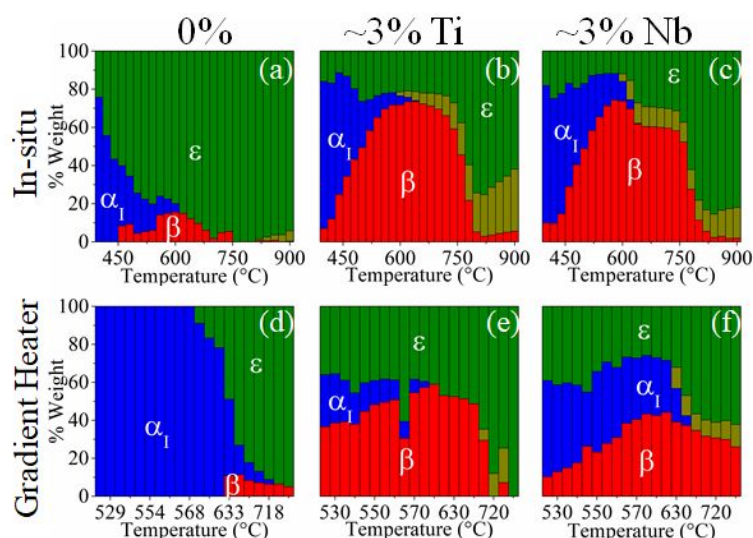
Fig. 5. Phase quantification of XRD from (a-c) the in-situ heating and (d-f) gradient heating of pristine and substituted LiVOPO$_4$·2H$_2$O in He showing how transition-metal substitution affects the amount of each phase formed.
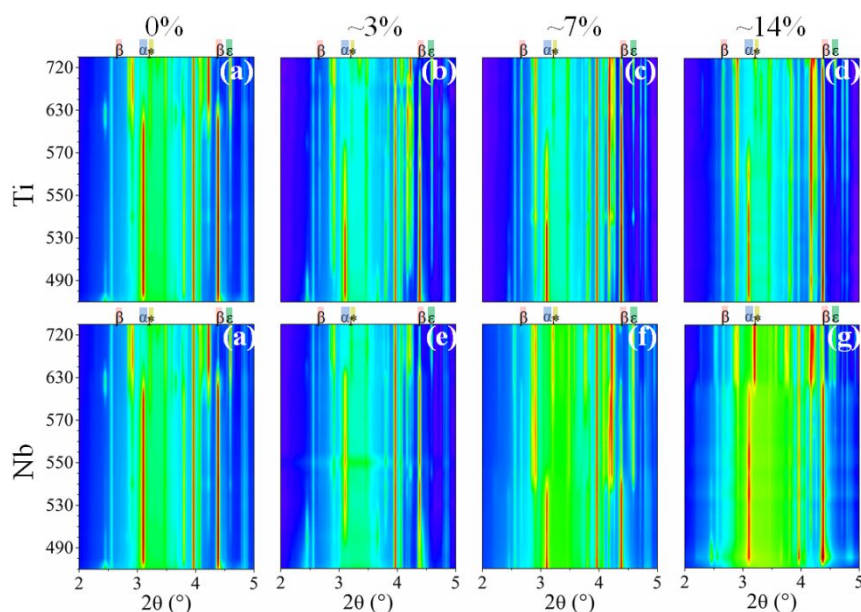
Fig. 6. XRD from the gradient heater method in He of (a) pristine, (b-d) Ti- and (e-g) Nb-substituted LiVOPO$_4$·2H$_2$O (λ = 0.2410 Å).

Thermal transformation of LiVOPO$_4$·2H$_2$O into β- and ε-LiVOPO$_4$

We have shown in a previous study that in-situ heating with XRD of LiVOPO$_4$·2H$_2$O can be used to show the differences in the stability of the various polymorphs of LiVOPO$_4$.[20] Here, we conducted a similar study, this time utilizing both in-situ heating with XRD and a novel technique using a gradient heater. The gradient heater approach is a tool for synthesis that enables the collection of crystallographic data from a reaction at a variety of temperatures simultaneously. The details for this novel technique are published elsewhere.[54]

Qualitatively, both techniques in He (Fig. 4) show that the material transforms with the trend of LiVOPO$_4$·2H$_2$O → α$_I$ → β → ε, with the substituted samples containing more β-LiVOPO$_4$ than the pristine. To better understand these transitions, we used Rietveld refinement to quantify the amount of each phase present at each temperature (Fig. 5). First, we observe that the transition temperatures are similar between the in-situ and gradient heater methods. Both methods also show that the amount of β-LiVOPO$_4$ increases with substitution, peaking at ~600 °C. The major difference is that we measure ~70% β-LiVOPO$_4$ at 600 °C for both Ti- and Nb-substituted LiVOPO$_4$ using the in-situ heating method while we only measure ~40-60% β-LiVOPO$_4$ in the gradient heater method. Although there is a disparity in the exact amount, both methods show that Ti- and Nb-substitution cause the formation of β-LiVOPO$_4$ over ε-LiVOPO$_4$. A similar study was conducted in O$_2$ (**Error! Reference source not found.** & **Error! Reference source not found.**), but these heating runs resulted in the samples transforming into
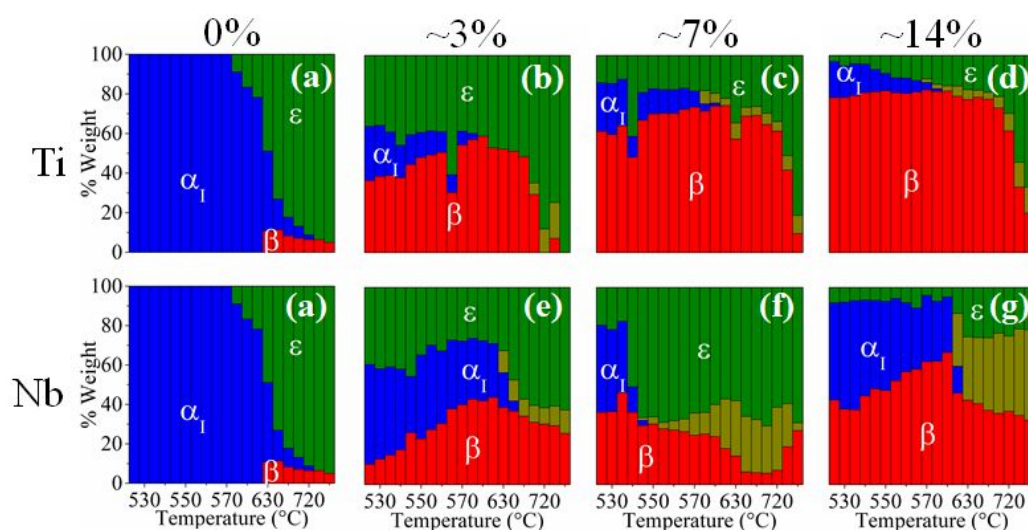

Fig. 7. Phase quantification of the XRD of (a) pristine, (b-d) Ti- and (e-g) Nb-substituted LiVOPO$_4$·2H$_2$O using the gradient heater method in He showing how increasing the amount of transition-metal substitution affects the amount of each phase formed.

ARTICLE

highly-pure β-LiVOPO₄, with no other notable transitions occurring. Although this proves that it is still possible to synthesize highly-pure β-LiVOPO₄, it is difficult to show any differences in stability from this data. Thus, we will focus our discussion mainly on the data from LiVOPO₄·2H₂O heated in He.

Effects of substitution on the thermodynamic stability and formation of β- and ε-LiVOPO₄

In the previous section, we showed that the gradient heater method can be used to observe the various high-temperature transitions, and the data is comparable to what is observed using the in-situ method. For further studies on the rest of the substituted samples, this gradient heater method was chosen over the in-situ method due to the gradient heater method being a more rapid measurement technique, allowing for more samples to be analyzed during the limited time spent at the synchrotron. From the XRD data (Fig. 6), we can qualitatively observe that as the amount of Ti- or Nb-substitution increases, there is also an increase in the amount of β-LiVOPO₄. This is more clearly seen by looking at the phase quantification diagrams (Fig. 7), where the amount of β-LiVOPO₄ quickly increases as the amount of substitution also increases.

Aside from the LiVOPO₄, we also observe the formation of impurities (shown as the dark yellow phase in the phase quantification diagrams) as either LiVP₂O₇ or Li₂V₂(PO₄)₃. These impurities are only seen when heating the samples in a capillary (such as in the in-situ and gradient heater methods), and not seen when heating the powders in a larger quartz tube. We hypothesize that these impurities only formed due to the intense and direct heat used when heating samples in a capillary, which causes O-loss and V-reduction. We theorize this because LiVP₂O₇ and Li₂V₂(PO₄)₃ have average V oxidation states of 3+ and 3.5+, respectively, and P:O ratios of 1:3.5 and 1:4, respectively. These are much lower than LiVOPO₄, which has a V oxidation state of 4+ and a P:O ratio of 1:5. Luckily, the

impurities do not form when synthesizing the powders in the larger quartz tubes. We theorize this to be the case because the heat from the large tubes is less direct and more evenly dispersed, reducing the chance of large hotspots forming, which would result in significant O-loss and reduction of the oxidation states in the reducing atmosphere used.

Although these impurities affect the amount of each phase present, the trend still shows that the more Ti- or Nb-substitution present, the larger the amount of β-LiVOPO₄ relative to ε-LiVOPO₄. To estimate the dopability of Ti and Nb in two phases, we provided the dopant formation energies (E_f, Fig. 8). Pristine ε-LiVOPO₄ is 5.5 meV/atom higher in energy than β-LiVOPO₄. With an increase in doping ratio, the dopant formation energy per dopant decreases (see Fig. 8). Doping of Ti into β- and ε-LiVOPO₄ is predicted to be more favorable than Nb. This is in line with the experimental observations in Fig. 7, where the total area (amount) of Ti-doped β- and ε-LiVOPO₄ is much larger than Nb-doped analogues.

We have shown previously that one of the major factors in stabilizing either β- or ε-LiVOPO₄ is the presence of O-defects.[20] Specifically, ε-LiVOPO₄ forms in the presence of small amounts of O-vacancies. One consequence of this is that β-LiVOPO₄ can be transformed into ε-LiVOPO₄ if O-vacancies are generated. At high temperatures, this is possible due to small amounts of O-loss.

Fig. 9 shows the free energies of pristine and O-defective β- and ε-LiVOPO₄ with 12.5% Ti and Nb doping within a temperature range of 0-1000K. We also calculated the O-vacancy formation energy E_f for undoped and Ti- or Nb-doped LiVOPO₄. To simplify the analysis, we chose to compare the values at $\Delta\mu_O$ = -2.0 eV, which is the lower bound (high temperature or reducing atmosphere) to avoid LiVOPO₄ decomposition in Table 1. With Ti and Nb doping, the O vacancy formation energy generally decreases in both β- and ε-LiVOPO₄, which explains the appearance of larger fractions of both phases at lower temperatures in Fig 7.

The β-ε proportion and transition temperatures can be tuned by the substitution species (Ti or Nb) and doping ratios.
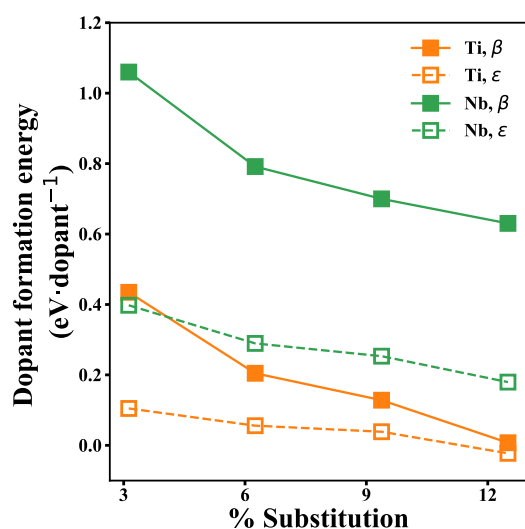

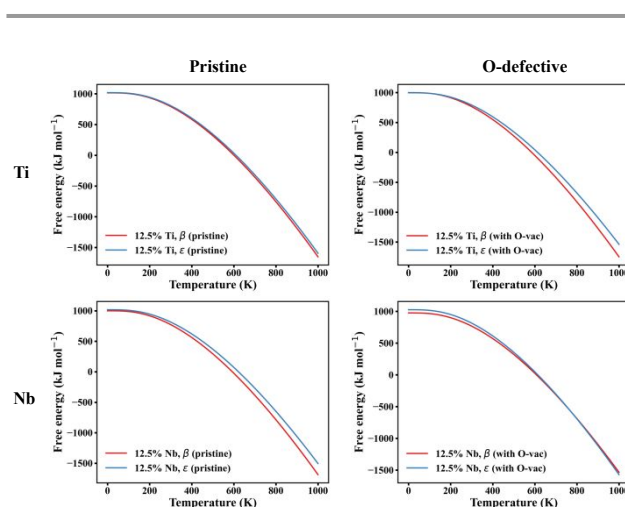Fig. 8. Dopant formation energy for 3%, 6%, 9%, 12% Ti and Nb-substituted LiVOPO₄

Fig. 9. Calculated Helmholtz free energy of 12.5% Ti and Nb-substituted β- and ε-LiVOPO₄ (pristine and O-defective).

Table 1. Summary of O-vacancy formation energies at $\Delta\mu_O$ = -2.0 eV.

Dopant	O-vac, Ef (eV)	0%	3%	6%	9%	12%
Nb	β-Nb	0.90	0.84	0.81	0.77	0.88
	ε-Nb	0.75	0.50	0.72	0.58	0.79
	ΔE_f of Nb (β-ε)	0.15	0.34	0.09	0.19	0.09
Ti	β-Ti	0.90	0.86	0.84	0.82	1.16
	ε-Ti	0.75	0.51	0.51	0.51	0.59
	ΔE_f of Ti (β-ε)	0.15	0.35	0.33	0.31	0.57

We found the effect of O vacancy is opposite in Ti and Nb doped LiVOPO$_4$ as shown in Fig 9. For Ti-doped LiVOPO$_4$, O vacancies help to stabilize β-phase at high temperatures through a larger free energy difference, which is also reflected in the large area of β phase in Fig. 7(d). For Nb, the opposite trend is true. The small ΔE_f(β-ε) after introducing O vacancies indicate that both β and ε can co-exist at a wide temperature range. For example, with 6% Nb substitution, a very small ΔE_f(β-ε) of 0.09 eV makes β-ε transition easier than 6% Ti, which matches with observed large area of ε-phase in Fig 7(f).

These calculations show that Ti- and Nb-substitution can tune β-ε transition with the existence of O vacancies in different ways and stabilize β-LiVOPO$_4$. We can experimentally show the delay in formation of O-vacancies using thermogravimetric analysis (TGA). Since O-vacancies form via the release of O$_2$, the formation of these O-vacancies will be accompanied by a weight drop (Fig. 10a). Note that the values in the TGA thermogram are relative masses, meaning 100% mass is set at 600 °C. This temperature was chosen since above this temperature is where
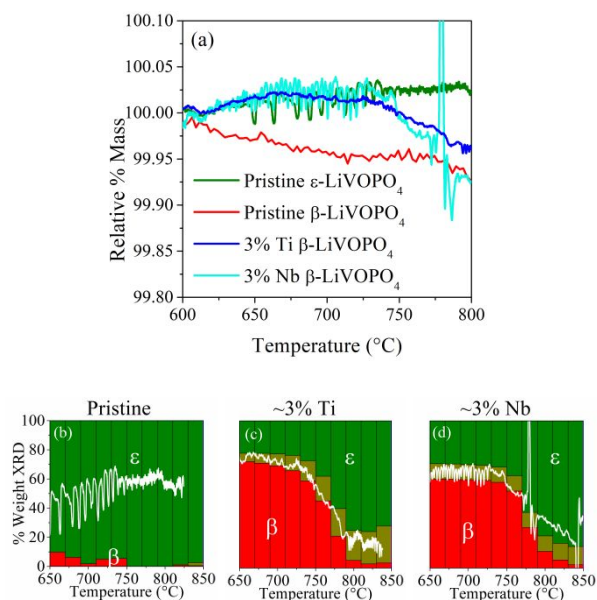
the β → ε transition occurs. The samples also adsorb small amounts of water from the air, which skews the low-temperature weight losses if we set 100% mass at room temperature.

We observe that the pristine ε-LiVOPO$_4$ does not have any weight loss at high temperatures. This is because it has already generated O-vacancies during its synthesis. On the other hand, the pristine β-LiVOPO$_4$ experiences a steady weight loss starting from 600 °C until around 750 °C. This coincides with the β → ε transition which we observed using in-situ heating with XRD in our previous report.[20] If we then compare the pristine β-LiVOPO$_4$ with either of the substituted β-LiVOPO$_4$ samples, we will see that the weight loss does not occur until a much higher temperature (~725 °C). If the TGA thermograms are then overlaid with the phase quantification diagrams (Fig. 10b − d) from in-situ heating with XRD shown previously, we see that the weight loss matches exactly with the β → ε transition. These prove that the high amount of β-LiVOPO$_4$ in the substituted samples is due to the substituents delaying the formation of O-vacancies.

Synthesis of substituted β- and ε-LiVOPO$_4$

From the heating data discussed previously, we have determined that β-LiVOPO$_4$ can be synthesized at a high temperature in O$_2$, while ε-LiVOPO$_4$ can be formed at even higher temperatures in an inert atmosphere, such as He or Ar. The highest temperatures we can attain while maintaining good crystallinity are 600 °C in O$_2$ and 900 °C in Ar. Temperatures higher than these cause the material to either transform into an amorphous phase (in O$_2$, hypothesized to be a Li$_x$V$_2$O$_5$ melt) or simply melt (in Ar). Thus, these two temperatures will be used to synthesize the pure-phase β- and ε-LiVOPO$_4$ used for the rest of this study.
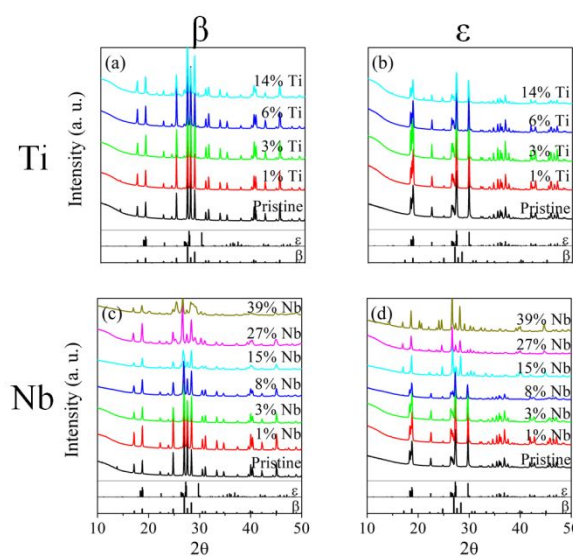

Fig. 10. Weight losses associated with O-loss seen in the (a) TGA of pristine and substituted LiVOPO$_4$. The (white lines) TGA thermograms are also overlaid on the (colored bars) in-situ heating with XRD data for (b) pristine, (c) 3% Ti-substituted, and (d) 3% Nb-substituted LiVOPO$_4$.

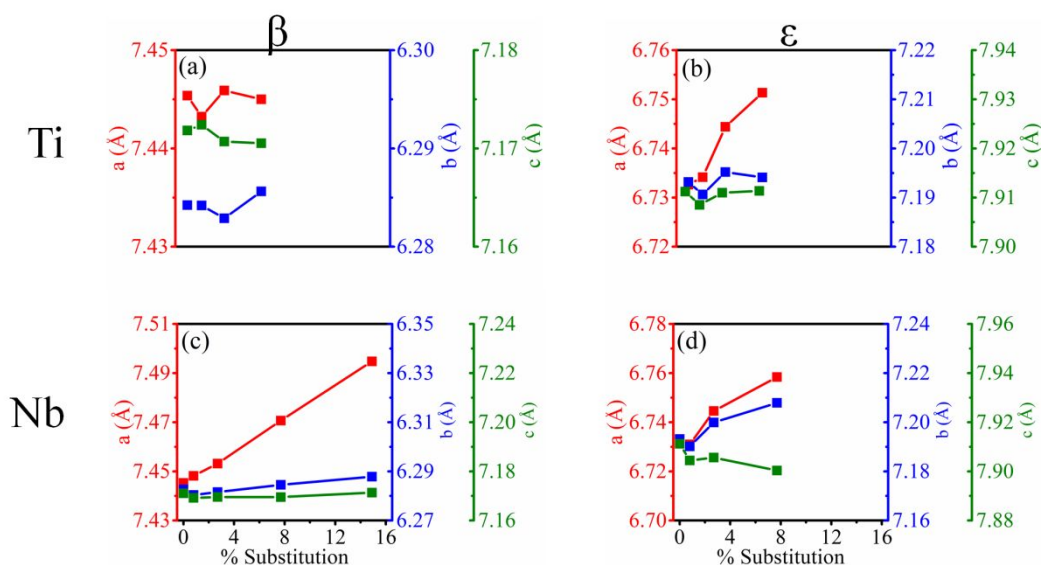Fig. 11. XRD of (top) Ti-substituted and (bottom) Nb-substituted (left) β- and (right) ε-LiVOPO$_4$ (λ=1.54053 Å).

Fig. 12. Changes in lattice parameters due to (top) Ti- and (bottom) Nb-substitution into (left) β- and (right) ε-LiVOPO₄ showing successful Ti- and Nb-substitution in both β- and ε-LiVOPO₄.

The resultant XRD after heating Ti-substituted LiVOPO₄·2H₂O at these temperatures (Fig. 11 top) show that we can get pure-phase β-LiVOPO₄ and ε-LiVOPO₄. Since these samples were synthesized in larger quartz tubes, we also did not form any LiVP₂O₇ or Li₂V₂(PO₄)₃ impurities present in the samples heated in capillaries. When forming β-LiVOPO₄, the 6% Ti-substituted sample contains ~5% β-VOPO₄, which increases to ~10% for the 14% Ti-substituted sample. The larger amount of β-VOPO₄ is due to the fact that the higher substituted samples are also more Li-deficient compared to the pristine samples, as shown earlier by ICP. As this is simply the delithiated form of β-LiVOPO₄, it is not considered an impurity. On the other hand, the ~14% Ti-substituted sample contains an impurity in the form ~10% LiTi₂(PO₄)₃. This impurity contains ~60% of the Ti within the sample, implying that the solubility limit of Ti in β-LiVOPO₄ via this method is <14%.

High-purity Ti-substituted ε-LiVOPO₄ can also be synthesized with <14% Ti substitution. This is because at ~14% Ti, there is the formation of ~6% LiTi₂(PO₄)₃ impurity, which corresponds to about 40% of the Ti detected by ICP.

Looking at their lattice parameters (Fig. 12 top), we observe that the Ti-substituted β-LiVOPO₄ experiences very small changes in the lattice parameters. On the other hand, the Ti-substituted ε-LiVOPO₄ experiences much larger changes in its lattice parameters, specifically in the a lattice parameter.

A similar heating protocol was also conducted with the Nb-substituted LiVOPO₄·2H₂O. The XRD of the post-heated samples (Fig. 11 bottom) show that β-LiVOPO₄ can be synthesized with high purity up to <27% Nb. At 27% Nb and above, many unknown impurities begin to form. On the other hand, pure-phase ε-LiVOPO₄ can be synthesized with substitution levels of only up to <15%. This is because at ~8% Nb-substitution, only ~90% of the sample is ε-LiVOPO₄, with the remainder being β-LiVOPO₄. Further increasing the Nb-content to ~15% results in ~80% β-LiVOPO₄. At substitution levels >15%, we also see the formation of LiVNb(PO₄)₃ as an impurity.

Looking at their lattice parameters (Fig. 12 bottom), we see that the a lattice parameter for Nb-substituted β- and ε-LiVOPO₄ also increases the most compared to the other lattice parameters. Altogether, we can synthesize phase-pure β- and ε-LiVOPO₄ which all exhibit consistent changes in their lattice parameters as the amount of substitution increases. These suggest that Ti- and Nb-substitution into β- and ε-LiVOPO₄ are successful.

We further show this by comparing the experimental volume changes with theoretical modelled volume changes expected to occur when substituting either Ti or Nb into LiVOPO₄. This comparison may be considered more accurate than comparing individual lattice parameter changes, especially for the triclinic structure, since volumes will include the effects of changes in the angles of the unit cell. This comparison of the different unit cell volumes calculated from XRD (Fig. 13a) show an increase in the overall volume as the amount of Ti- and Nb-substitution increases. The samples with the smallest change in volume were the Ti-substituted β-LiVOPO₄, while the Nb-substituted ε-LiVOPO₄ resulted in the largest increase in volume. Predicted unit cell volumes upon substitution (Fig. 13b) predict increases in the volumes of all the Ti- and Nb-substituted samples, which fits the experimental data.
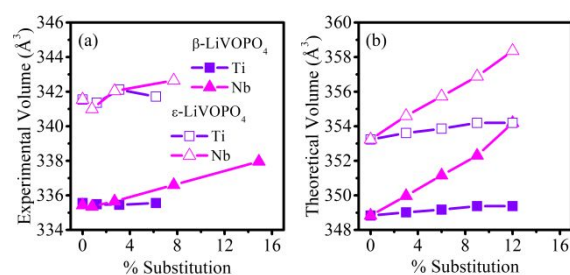

Fig. 13. Comparison of (a) experimental and (b) calculated volumes for (violet) Ti- and (magenta) Nb-substituted (solid) β- and (open) ε-LiVOPO₄ showing successful Ti- and Nb-substitution in both β- and ε-LiVOPO₄.

Additionally, it predicts that Ti-substituted β-LiVOPO$_4$ would experience a very small change in volume, which matches with the observed experimental volume changes. It also predicts the larger volume change due to Nb-substitution, which fits our experimental results. These increases in volume are due to the larger size of the Ti^{4+} and Nb^{5+} substituents (with ionic radii of 0.61 Å and 0.64 Å, respectively) compared to the that of V^{4+} (0.58 Å).[71] Note that the base theoretical volumes are larger than the experimental values. These differences are expected when comparing the theoretical calculations with the experimental values, which we have reported previously.[21] More importantly, the differences in the volumes induced by substitution predicted by our calculations match well with what is seen experimentally.

Overall, we show that we can successfully synthesize Ti- and Nb-substituted β- and ε-LiVOPO$_4$, up to a certain extent. We show that Ti-substitution into both β- and ε-LiVOPO$_4$ are successful with up to ~6% substitution. Above these levels, we start seeing the formation of Ti-rich impurities. Similarly, Nb-substitution into both β- and ε-LiVOPO$_4$ is possible up to ~15% for β-LiVOPO$_4$ and ~8% for ε-LiVOPO$_4$. Above ~8% substitution, the ε-LiVOPO$_4$ is still substituted, but is no longer phase-pure ε-LiVOPO$_4$ as there is also a large amount of substituted β-LiVOPO$_4$ present within the material. Above these levels, we also see the formation of various impurities.

Probing the effects of substitution on the initial electrochemical performance of LiVOPO$_4$ using X-ray Absorption Spectroscopy

Once the specific conditions for synthesizing pure-phase β- and ε-LiVOPO$_4$ have been identified, their electrochemical performance can be tested. The first full cycle of each substituted sample (Fig. 14) can be used to immediately ascertain if the substitution had a positive or negative effect on the electrochemical performance. For Ti-substituted β-LiVOPO$_4$, we see that increasing the amount of substitution also increases the initial capacity by lengthening the high-voltage plateau. On the other hand, the Ti-substituted ε-LiVOPO$_4$ samples perform slightly worse than the pristine ε-LiVOPO$_4$. For Nb-substituted β-LiVOPO$_4$, the 1% sample has the best performance, followed by the 3% Nb sample, then the pristine sample. These improvements were also due to the lengthening of the high-voltage plateau. For Nb-substituted ε-LiVOPO$_4$, the 1% Nb and the pristine samples roughly have the same electrochemical performance, while the 3% Nb sample performed poorly, due to a much shorter low-voltage plateau.

Ex-situ X-ray absorption spectroscopy (XAS) of cycled LiVOPO$_4$ is a powerful tool to understand the processes occurring during this initial cycling because it can measure the oxidation states of the V, Ti, and Nb. These would allow us to determine which species are causing changes in capacity. First, we note that the Ti K-edge (Fig. 15 top) shows that the Ti is in the 4+ oxidation state, since the edge and pre-edge features of the Ti-substituted β- and ε-LiVOPO$_4$ both match those of TiO$_2$. We do also not expect Ti to be redox active, since the Ti^{3+}/Ti^{4+} redox voltage is at 1.51 V. This agrees with the fact that we do not see any redox reactions not associated with LiVOPO$_4$. While we were unable to measure Ti redox during cycling due to its
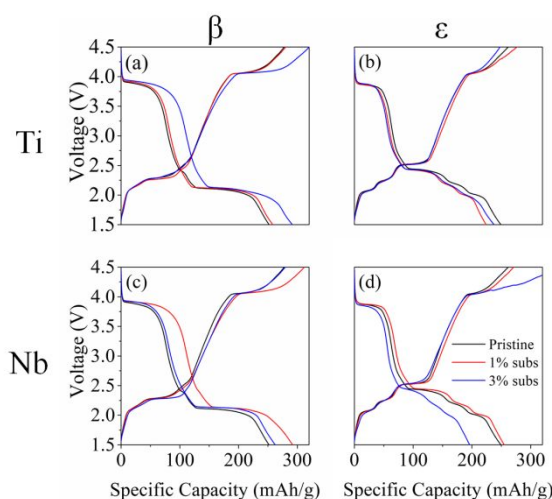

Fig. 14. Changes in the 1st cycle electrochemical performance at C/20 due to transition-metal substitution in LiVOPO$_4$.

low concentration within the electrodes, we assume this low concentration of Ti to have marginal capacity contribution if ever it was electrochemically active.

On the other hand, Nb XAS shows that the Nb is in the Nb^{5+} state, since its edge matches that of Nb$_2$O$_5$ (Fig. 15 bottom). During cycling, we also note that the Nb XAS does not shift, meaning Nb remains in the 5+ state and does not contribute to the overall capacity.

Thus, we would expect that all the differences in capacity should be due to changes in the V oxidation state. Looking at the V XAS (Fig. 16), we observe that all the uncycled samples have a V oxidation state of 4+, which is expected of LiVOPO$_4$. All the phases also reach V^{3+} on the first discharge going from OCV to 1.5 V, which is expected since intercalation at the low-voltage region is facile.[17, 20] Thus, any improvements in the electrochemical performance would focus mainly on the high-voltage region. As expected, the first charge up to 4.5 V is where a lot of the differences begin to appear. Pristine β-LiVOPO$_4$ does not reach full V^{5+}, which agrees with the fact that we do not attain full theoretical capacity. On the other hand, the 1% Ti
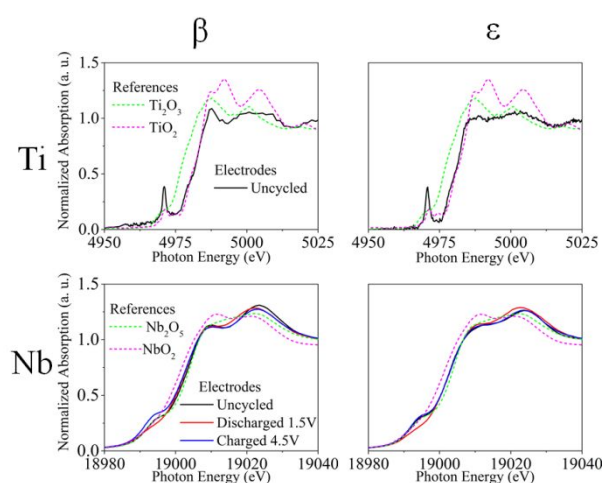

Fig. 15. Ti and Nb XAS in substituted β- and ε-LiVOPO$_4$ showing Ti in the 4+ state and Nb in the 5+ state.
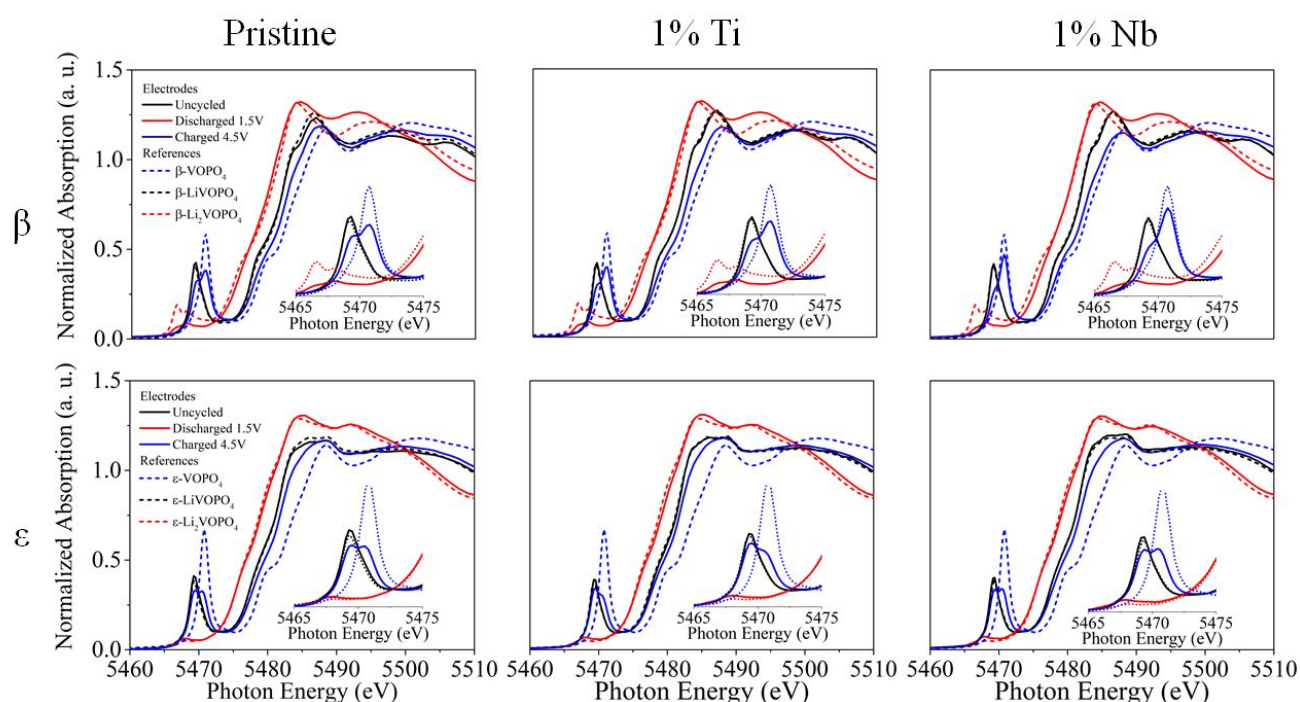
ARTICLE

Fig. 16. V K-edge XAS of pristine and 1% substituted β- and ε-LiVOPO$_4$ showing how transition-metal substitution affects the V-redox, mainly in the V^{4+}/V^{5+} redox couple.

sample charged to 4.5 V has a higher amount of V^{5+} compared to the pristine, indicating that the Ti improved the high-voltage capacity. This is in agreement with the 1st cycle data discussed previously. The same observation can be made with the 1% Nb β-LiVOPO$_4$ sample, which has an even higher capacity than the 1% Ti sample and has a larger amount of V^{5+}. Looking at ε-LiVOPO$_4$, we see that the pristine, 1% Ti, and 1% Nb samples all have similar amounts of V^{5+} when charged to 4.5V, which fits with the observation that they all have similar 1st cycle capacities.

Thus, we see here that Ti and Nb improve the initial electrochemical performance by improving the high-voltage capacity of β-LiVOPO$_4$. On the other hand, substitution does not greatly affect the ability of ε-LiVOPO$_4$ to reach V^{5+}, which explains the limited change in its initial cycling performance.

Effect of substitution on the long-term cycling capability and rate-performance of β- and ε-LiVOPO$_4$

The effect of substitution is not only limited to the initial capacities. Long-term cycling (Fig. 17) shows that, the pristine samples quickly fade in capacity (whether it is β- or ε-LiVOPO$_4$). On the other hand, all the substituted samples tested (with substitution levels ranging from 1% to 3%) resulted in significantly improved long-term cycling performance, regardless of polymorph.

For Ti-substituted β-LiVOPO$_4$, the 3% substituted sample performed the best, followed by the 1% Ti sample and then pristine. This trend matches the initial capacities of Ti-substituted β-LiVOPO$_4$, suggesting that the improved cycling

performance may be related to the improved high-voltage capacity. Looking at the voltage profiles over several cycles (Fig. 18), we see that capacity fade in the Ti-substituted β-LiVOPO$_4$ is less in the high-voltage region compared to the pristine. Thus, we conclude that the Ti improves the cycling performance of β-LiVOPO$_4$ by improving the electrochemical performance in the high-voltage region.
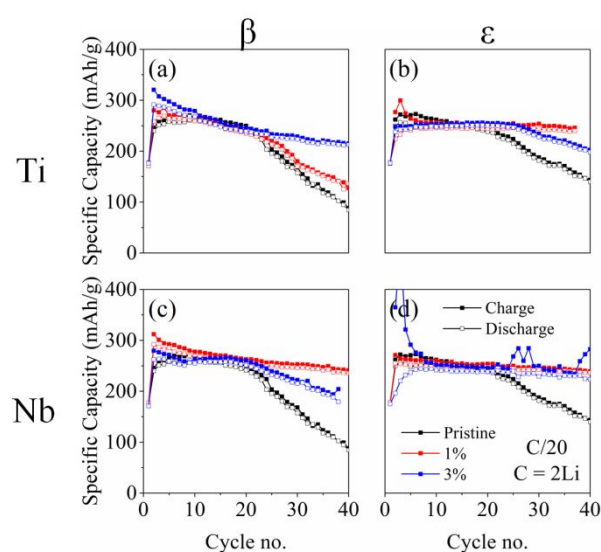

Fig. 17. Long-term cycling data showing improvements in capacity retention due to transition-metal substitution.

There is no change in the initial cycling performance due to substitution within Ti-substituted ε-LiVOPO$_4$. However, long-term cycling data shows that the 1% Ti sample has the best cycling performance, followed by the 3% Ti sample, then the pristine. The voltage profiles of these samples show that substitution reduces the washing out of the low-voltage region while also maintaining the capacity in the high-voltage region. These all clearly show that Ti-substitution into ε-LiVOPO$_4$ significantly improves the overall electrochemical performance.

For Nb-substituted β-LiVOPO$_4$, the 1% substituted sample retains the most capacity over several cycles, followed by 3% Nb and the pristine. This trend also matches with the initial capacities of Nb-substituted β-LiVOPO$_4$. Looking at the voltage profiles over several cycles, we see that the 1% Nb sample retains its large capacity by stabilizing both the high- and low-voltage regions. The 3% Nb sample maintains a stable high-voltage plateau but slowly loses capacity in the low-voltage region, which explains why it performs poorly compared to the 1% Nb sample.

Conversely, the Nb-substituted ε-LiVOPO$_4$ shows that both the 1% and 2.5% Nb samples experience very little capacity fade. Although the 2.5% Nb sample does begin with the lowest capacity due to a shorter low-voltage region, it quickly recovers and attains a similar capacity to the 1% Nb sample. The voltage profiles over several cycles show that the high- and low-voltage plateaus do not significantly change over several cycles for the substituted samples.

As mentioned previously, one major goal for transition-metal substitution is the improvement of the rate capability of LiVOPO$_4$. A comparison of the capacities at different C-rates of the best performing samples for each substituent and polymorph (Fig. 19) shows that all the substituted samples have superior rate performance compared to the pristine. For β-LiVOPO$_4$, the 1% Nb-substituted sample resulted in the overall best rate capability. Although the 3% Ti-substituted sample also had a good rate capability, its performance significantly dropped at rates higher than C/10. For ε-LiVOPO$_4$, both 1% Ti-substituted and 1% Nb-substituted samples performed similarly. It should be noted that there were some charging

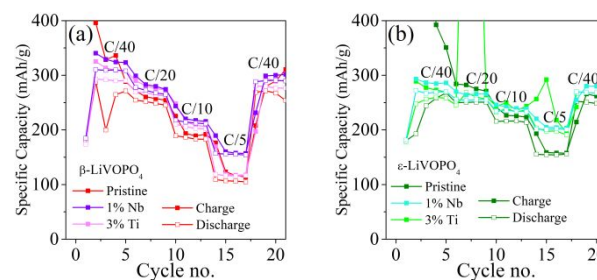Fig. 19. Rate performance comparing pristine with the best performing substituted samples of (left) β- and (right) ε-LiVOPO$_4$ (C = 305 mAh/g).

issues with the 1% Ti-substituted ε-LiVOPO$_4$ and low-rate cycling in the pristine ε-LiVOPO$_4$ sample. This was occasionally observed within the samples heated at 900 °C, suggesting that this excessively high temperature may have some detrimental effects on the overall cycling performance of the materials.

Probing the causes of the improved electrochemical performance

To explain the overall improved electrochemical performance, we conducted cyclic voltammetry (CV) experiments (Fig. 20a – c) to estimate the overall Li$^+$ diffusion coefficients (Fig. 20d). The specifics related to these calculations for LiVOPO$_4$ are discussed elsewhere.[21] The 1% Nb- and 3% Ti-substituted β-LiVOPO$_4$ samples were selected for this test because they were the best-performing Ti- and Nb-substituted samples. We also tested the pristine sample to serve as a baseline. We did not test ε-LiVOPO$_4$ as the initial cycling data and XAS data showed that there were no significant changes with the initial cycling of ε-LiVOPO$_4$.

The estimated overall Li$^+$ diffusion coefficients from CV (D_{CV}) during discharge show that the low-voltage region has significantly larger Li$^+$ diffusivity compared to the high-voltage region. This explains why the material easily reaches V^{3+} at 1.5 V but cannot fully reach V^{5+} at 4.5 V. Additionally, we see that both substituted samples exhibited superior values for D_{CV} compared to the pristine, especially in the high-voltage region where most of the improvements in capacity occur. Thus, the
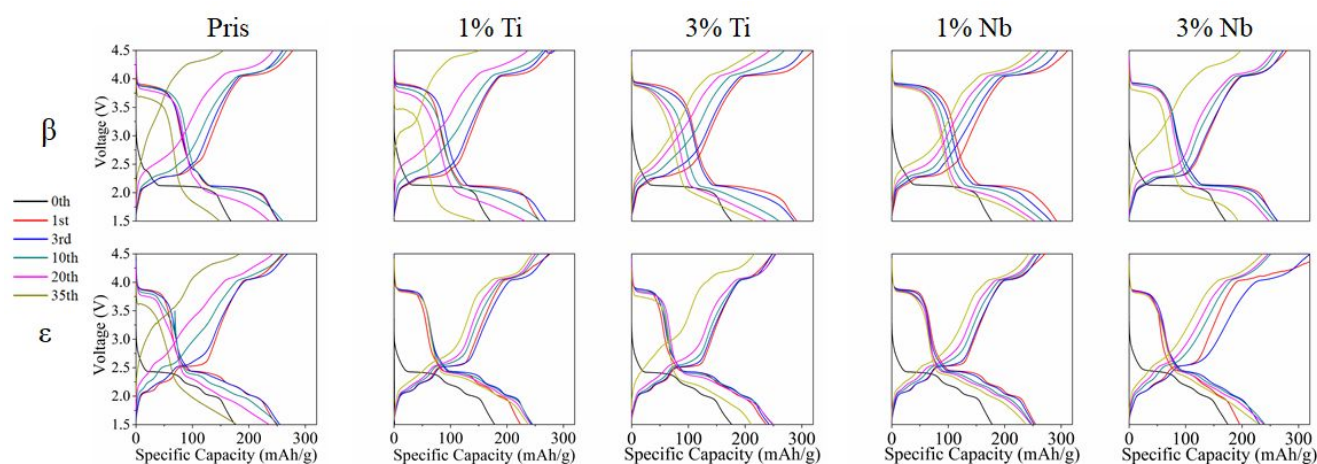
Fig. 18. Voltage profiles over several cycles of pristine, Ti-substituted, and Nb-substituted LiVOPO$_4$ showing how substitution affects capacity fade in the high- and low-voltage regions.
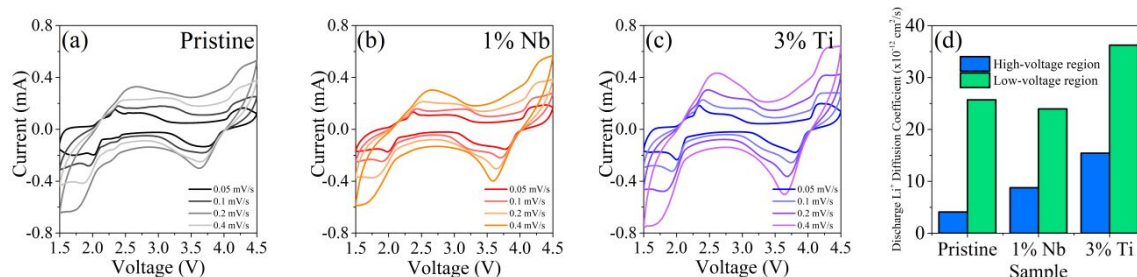
Fig. 20. CV data for (a) pristine, (b) 1% Nb-, and (c) 3% Ti-substituted LiVOPO$_4$, with the (d) estimated overall Li$^+$ diffusion coefficients during discharge.

improved electrochemical performance can be attributed to Ti- and Nb-substitution improving the overall Li$^+$ diffusion.

We then go a step further and use electrochemical impedance spectroscopy (EIS) in order to identify the sources of this improved overall Li$^+$ diffusion. The samples were tested at the end of charge (4.0 V), middle of the discharge (3.4 V), and at the end of discharge (1.6 V) to represent the impedances within VOPO$_4$, LiVOPO$_4$, and Li$_2$VOPO$_4$, respectively. Qualitatively, the substituted samples exhibit smaller overall impedances compared to the pristine sample, as shown by the overall smaller diameters of the semicircles in the Nyquist plots (Fig. 21a – c). We can quantitatively measure this improvement by modelling the Nyquist plots using a modified Randles circuit (Fig. 21d). R$_s$ represents the internal resistance of the cell, which is associated to the general resistances within the cell due to the inherent resistances within all the materials encompassing the cell. R$_{ct}$ represents the charge-transfer resistance, which is associated with the exchange of electrons as the Li$^+$ transitions from the electrolyte onto the surface of the active material (and vice versa). A constant phase element (CPE) is placed in series

with the R$_{ct}$ to represent the Warburg impedance, which can be used to model the diffusion of Li$^+$ within the bulk of the active material. Ideally, this Warburg impedance should be a straight line with an angle of 45 ° in the Nyquist plot. However, our experimental data shows deviations from this angle. Thus, a CPE is instead used in the model to account for this deviation. The extent of this deviation can be quantified using the variable α (**Error! Reference source not found.**), which is a measure of how close a CPE is to other electronic components. As α approaches 0.5, the CPE approaches the ideal behaviour of a Warburg impedance and the angle of the Warburg portion in the Nyquist plot approaches 45 °. Note that the deviations are not significantly large, with the exception of the 4.0 V sample containing 1% Nb-substitution. Thus we can conduct bulk diffusion calculations using all the Warburg impedance data sets with the exception of the 4.0 V sample containing 1% Nb-substitution. Finally, the CPE parallel to R$_{ct}$ represents the electric double layer (EDL) on the surface of the active materials. A CPE is used here instead of a capacitor due to the
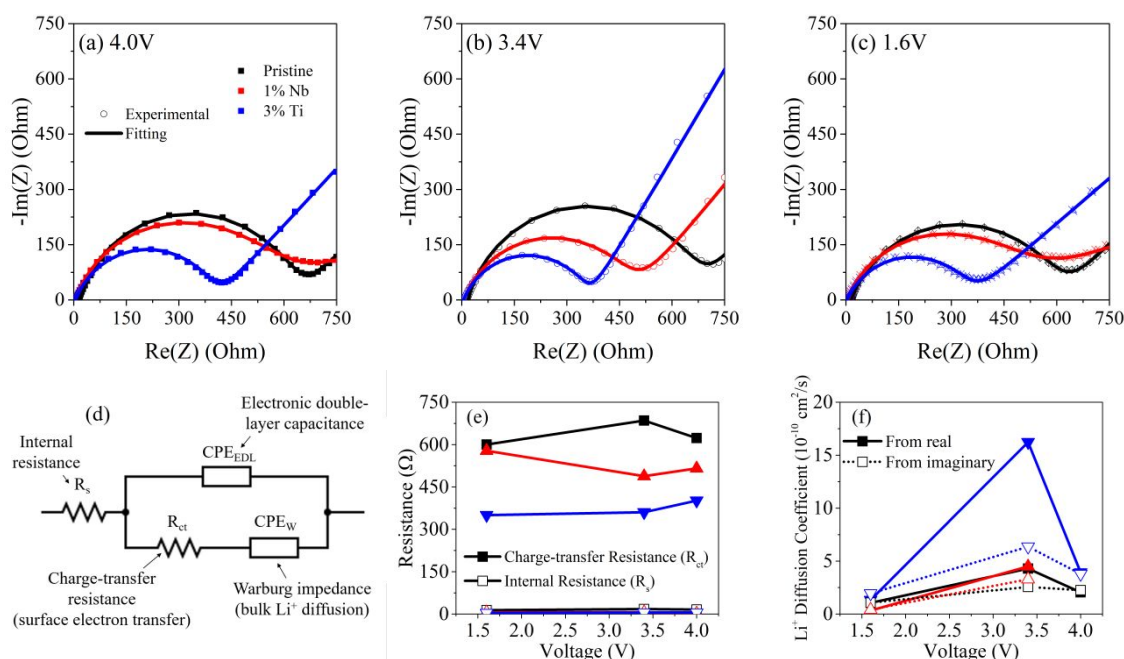

Fig. 21. EIS data showing a comparison between the experimental and fitted Nyquist plots at different charge states: (a) 4.0V, (b) 3.4V, and (c) 1.6V. The fittings used (d) a modified Randles circuit, which was then used to (e) calculate the series and charge-transfer resistances The Warburg diffusion region of the EIS plots were also (f) used to estimate the bulk Li$^+$ diffusion coefficients.
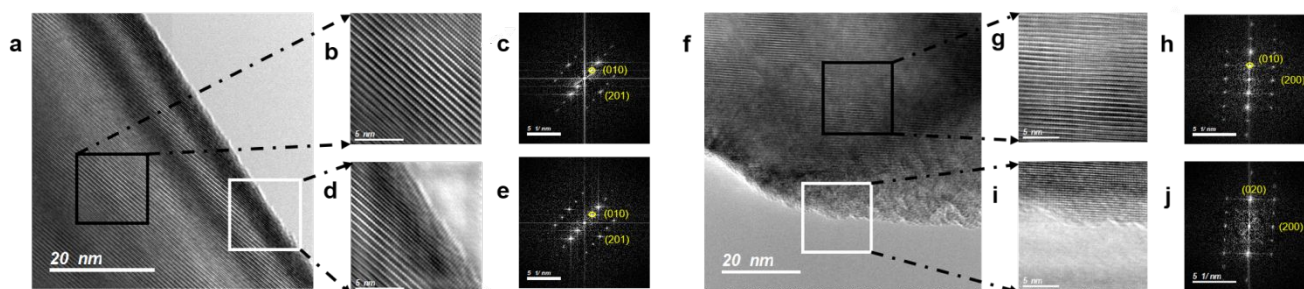
Fig. 22. Comparison of structures of the bulk and surface in pristine and 3%Ti substituted β-LiVOPO$_4$. HRTEM images of (a) the pristine β-LiVOPO$_4$ particle, with (b) the magnified view of the bulk region and (c) its corresponding FFT image. This can be compared to (d) the magnified view of the surface region of the pristine sample with (e) its corresponding FFT image. Similar images are taken for the (f) Ti substituted β-LiVOPO$_4$ particle, with (g) the magnified view of the bulk region and (h) its corresponding FFT image. Finally, (i) the magnified view of the surface region of the Ti-substituted sample, with (e) its corresponding FFT image.

EDL of the material not acting as an ideal capacitor, which is often the case in Li-ion batteries.

The values for all these model components can be estimated by creating a fit with the EIS data (solid lines in Fig. 21a – c). The analysis will focus on the changes to the values for R_s, R_{ct} (Fig. 21e), and the bulk Li$^+$ diffusion coefficient calculated using the Warburg impedance (D_W). R_s shows if transition-metal substitution will cause any significant changes in the electronic resistance of the active material. R_{ct} shows changes in the ease of transfer of electrons during the insertion of Li$^+$ form the electrolyte onto the surface of the active material (or for the reverse reaction). Finally, D_W shows changes in ability of Li$^+$ to diffuse within the bulk of the active material. D_W is estimated using the Warburg coefficient based on the method described by Ho et al.[58] Since there is a slight deviation in the calculated Warburg coefficients due to the non-deal Warburg behaviour, the Warburg coefficients are estimated separately using both the real and imaginary impedances. Values of D_W using both forms of impedances are reported here.

In general, the values for both R_s and R_{ct} are lower for the substituted samples compared to the pristine (Fig. 21e). However, the values for R_s are insignificant relative to R_{ct}, meaning charge-transfer is a more significant limiting factor than the inherent resistance of the cell. We also see that both Ti- and Nb-substitution improve the charge-transfer resistance, which would partially explain the improved electrochemical performance of the substituted samples. Looking then at the bulk diffusion coefficients, we see that Ti-substitution significantly improves the bulk Li$^+$ diffusivity while Nb-substitution does not. However, note that these values are in the range of 10^{-10} cm^2/s, much larger than the overall Li$^+$ diffusion coefficient (D_{CV}) of 10^{-12}. Since the overall Li$^+$ diffusion is a combination of bulk Li$^+$ diffusion and Li$^+$ charge-transfer at the surface, our data suggests that charge-transfer is the overall rate-limiting step during discharge. This fact is in agreement with the CV data, which suggests that the electrochemical reaction is quasi-reversible. We say this because as the scan rate is increased, the electrochemical peaks shift, which is indicative of an electrochemically quasi-reversible reaction. In other words, the CV data suggests that the charge-transfer at the surface is possibly slower than the diffusion of Li$^+$ within the bulk, which matches our EIS data.

Thus, improvements in the electrochemical performance are more likely to be the result of improvements in the charge-transfer occurring at the surface of the active materials. This suggests that there may be some form of improved interface between the active material and the electrolyte, which improves the transition of Li$^+$ ions from the electrolyte onto the surface of the active material (or vice versa).

To confirm the presence of such an interface, high resolution transmission electron microscopy (HRTEM) images were taken comparing the pristine and the 3% Ti-substituted β-LiVOPO$_4$ samples. The 3% Ti-substituted sample was selected among all the samples as this resulted in the overall largest drop in the charge-transfer resistance. As can be seen from the HRTEM image of the pristine β-LiVOPO$_4$ powder (Fig. 22a), there is no difference between the bulk region and surface areas, which could be verified by the magnified view and corresponding diffractograms (fast Fourier transform) in the bulk region (Fig. 22b and Fig. 22c) and surface area (Fig. 22d and Fig. 22e). However, once substituted with Ti, we could clearly observe a change at the surface (Fig. 22f). The HRTEM image in the bulk region of the Ti-substituted β-LiVOPO$_4$ (Fig. 22g) shows the alternate bright and faint contrast of the (010) planes. The HRTEM image at the surface area shows the "all bright" contrast of the (020) planes (Fig. 22i). Corresponding diffractograms (Fig. 22h and Fig. 22j) also confirm this by the disappearance of the (010) spot in the surface region, which may be caused by Ti substitution. This shows that there is indeed the formation of a surface layer on the transition-metal substituted LiVOPO$_4$ which may have a different composition compared to the bulk. This new surface layer may be the cause for the improved charge transfer during cycling.

Discussion

We have previously shown that LiVOPO$_4$·2H$_2$O is a good precursor to study the differences in thermodynamic stability and electrochemical performance between β- and ε-LiVOPO$_4$, two of the most stable polymorphs of LiVOPO$_4$. We have also previously shown that the major difference between the two phases is the fact that ε-LiVOPO$_4$ becomes more stable than β-LiVOPO$_4$ in the presence of O-vacancies.[20, 21] We utilize similar techniques in this study, where we show that Ti- and Nb-substitution stabilize β-LiVOPO$_4$ over ε-LiVOPO$_4$. Our calculations show that this is attributed to the substituents

inhibiting the formation of O-vacancies, and not due to changes in the inherent thermodynamic stability of either phase during substitution. That is, Ti- and Nb-substitution impede the formation of O-vacancies, which inhibits the $\beta \rightarrow \varepsilon$ transition. We showed this experimentally by observing the $\beta \rightarrow \varepsilon$ transition utilizing XRD taken from both the in-situ heating and the novel gradient heating methods, as well as TGA to observe the drop in weight due to O-loss.

Overall, β-LiVOPO$_4$ can be synthesized from LiVOPO$_4 \cdot$2H$_2$O by heating the precursor at 600 °C in O$_2$. Temperatures higher than this causes LiVOPO$_4$ to react to form an amorphous melt, hypothesized to be Li$_x$V$_2$O$_5$. Conversely, ε-LiVOPO$_4$ can form by annealing the precursor at a high temperature (in this case, 900 °C in Ar). Above this temperature, LiVOPO$_4$ begins to melt. The formation of impurities also limits our ability to introduce substituents into LiVOPO$_4$. High amounts of Ti results the formation of LiTi$_2$(PO$_4$)$_3$. Limits to the amount of Nb-substitution in LiVOPO$_4$ are mainly due to the formation of unknown impurities or the material with high levels of substitution melting before O-vacancies can be generated. Overall, we show that it is possible to substitute Ti into LiVOPO$_4$ with up to ~6% Ti in both β- and ε-LiVOPO$_4$. Similarly, up to ~15% Nb can be substituted into β-LiVOPO$_4$ and <8% into ε-LiVOPO$_4$.

We focused our electrochemical testing on the samples with <5% substitution, namely the pristine, 1%, and 3% substituted samples. Literature generally shows that the low-substituted samples have superior electrochemical performance compared to the highly substituted samples, even for LiVOPO$_4$.[38-41] The samples with low levels of substitution also generally resulted in more pure-phase products, eliminating the possible effects of unseen impurities or small amounts of β-LiVOPO$_4$ appearing in the ε-LiVOPO$_4$.

Firstly, XAS confirms that Ti is in the 4+ oxidation state while Nb is in the 5+ state. Additionally, it shows that Nb is not electrochemically active. We also do not expect Ti redox to contribute to the overall capacity due to its low redox potential and low concentration. Thus, any capacity changes are due solely to V redox. XAS also shows that both Ti- and Nb-substitution cause an improvement in the ability of β-LiVOPO$_4$ to reach V^{5+}. However, they do not significantly improve the amount of V^{5+} in ε-LiVOPO$_4$.

Interestingly, both Ti- and Nb-substitution improve the long-term cycling of LiVOPO$_4$, regardless of polymorph, substituent used, or whether it improved the initial capacity or not. However, different levels of substitution also result in different effects on the long-term cycling, just as it did with the initial capacity. The rate capabilities of the substituted samples were also superior to those of the pristine samples. It was also observed that the samples synthesized at 900 °C occasionally had charging issues, which we attribute to this high synthesis temperature. To our knowledge, no other report has discussed the electrochemical performance of LiVOPO$_4$ synthesized at such a high temperature (> 800 °C), so we currently are unsure why these charging issues are observed.

In order to understand the mechanisms behind the overall improvements in the electrochemical performance, various other tests were conducted comparing the pristine samples

with the substituted samples. The overall diffusion coefficient of Li$^+$ was estimated using CV and shown to improve with substitution. This directly explains the overall improved electrochemical performance of the substituted samples. EIS allowed us to go one step further and identify the various changes which may cause this improved overall Li$^+$ diffusion coefficient. We show that, although the internal resistances of the cells do decrease and the Ti-substituted samples do have improved bulk Li$^+$ diffusion coefficients, the main drivers for the improved electrochemical performances were the significant drops in the charge-transfer resistances upon substitution. This suggests the possible formation of a surface layer or coating that facilitates the transition of the Li$^+$ ion from the electrolyte to the active material and vice versa. We show that this is, indeed, the case in the Ti-substituted sample. HRTEM shows the formation of a surface phase corresponding to β-LiVOPO$_4$ missing the (010) planes in the Ti-substituted sample. This surface phase was not present within the pristine and possibly explains the overall improved electrochemical performance of the Ti-substituted samples. Although we do not have HRTEM images of the Nb-substituted samples, we hypothesize that it may have a similar surface layer.

The use of small amounts of substituents to improve the electrochemical performance via the formation of a surface layer is very similar to how Al is used in NCA.[72] This shows that low levels of substitution may be a viable method for the introduction of surface coatings.

While we were not the first to report on Ti-substitution in LiVOPO$_4$, the study by Lee *et al*. was only limited to cycling 1 Li in ε-LiVOPO$_4$.[40] They also show that Ti-substitution does improve the cycling capability of ε-LiVOPO$_4$, which is in agreement with our results. They attribute this to the improved overall kinetics upon substitution, which is in agreement with our results as well. Interestingly, when they substituted Ti into ε-LiVOPO$_4$, there is an increase in the peak intensities of their β-LiVOPO$_4$ side-products. This is in agreement with our results and predictions that Ti-substitution should stabilize β-LiVOPO$_4$ over ε-LiVOPO$_4$. This shows that our observations are not merely limited to Ti-substitution into LiVOPO$_4 \cdot$2H$_2$O. In their electrochemical testing, they also did not take into account the possible effects of this β-LiVOPO$_4$ phase on the electrochemical performance of ε-LiVOPO$_4$. Overall, we are able to expand upon their electrochemical study by showing that Ti-substitution has different effects on β-LiVOPO$_4$ compared to ε-LiVOPO$_4$. We also conducted our tests over the full 2-Li cycling window and showed other possible mechanisms involved in improving the capacity, namely the improved charge-transfer resistance and the presence of the surface layer.

There is also a rising interest in Nb-substitution into (Li)VOPO$_4$. This report adds to this group of studies by focusing on how Nb-substitution affects both major polymorphs over the full 2-Li cycling window, and gives some possible explanations for this improved electrochemical performance.

Conclusion

This study contributes to the overall literature of transition-metal substitution into $LiVOPO_4$ by showing the changes in the thermodynamic stability and electrochemical performance of β- and ε-$LiVOPO_4$ upon substitution of V with either Ti or Nb. Specifically, we show that both Ti- and Nb-substitution stabilize β-$LiVOPO_4$ by inhibiting the formation of O-vacancies. Thus, we are able to synthesize pure-phase, substituted β-$LiVOPO_4$ with varying amounts of substitution. Conversely, we can still synthesize pure-phase, substituted ε-$LiVOPO_4$, albeit at an increased temperature compared to the pristine. We have also shown that substitution is a promising method for improving the electrochemical performance of $LiVOPO_4$. With the exception of the 3% Nb-substituted ε-$LiVOPO_4$, all the substituents up to 3% either significantly improved or only slightly decreased the 1st cycle capacity of $LiVOPO_4$. Additionally, the 3% Nb-substituted ε-$LiVOPO_4$ sample quickly increased its capacity, matching the capacity of the other phases by the 6th cycle. Over several cycles, we have shown that all the substituted samples (even the 3% Nb-substituted sample) had better capacity retention and rate performance than the pristine for both β- and ε-$LiVOPO_4$. We showed that Nb was in the 5+ oxidation state and was not electrochemically active during cycling. Similarly, we show that Ti is in the 4+ oxidation state. Although we could not measure the oxidation state of Ti during cycling, do not expect it to be electrochemically active due to its low redox potential and low concentration. We show then that the improved electrochemical performance is due to an increase in the overall Li^+ diffusion coefficient, which is driven by a lower charge-transfer resistance. One possible cause of this improved resistance is the formation of a surface layer or coating which possibly facilitates the transfer of Li^+ from the electrolyte into the cathode and vice versa, which we confirmed to be present in the 3% Ti-substituted sample.

Conflicts of interest

There are no conflicts of interest to declare.

Acknowledgements

References

1. M. S. Whittingham, *Proceedings of the IEEE*, 2012, **100**, 1518-1534.
2. G. E. Blomgren, *Journal of The Electrochemical Society*, 2017, **164**, A5019-A5025.
3. M. S. Whittingham, *Chemical Reviews*, 2004, **104**, 4271-4302.
4. M. Armand and J. M. Tarascon, *Nature*, 2008, **451**, 652.
5. L. Lu, X. Han, L. Jianqiu, J. Hua and M. Ouyang, *Journal of Power Sources*, 2013, **226**, 272–288.
6. M. S. Whittingham, *Chemical Reviews*, 2014, **114**, 11414-11443.
7. V. Etacheri, R. Marom, R. Elazari, G. Salitra and D. Aurbach, *Energy & Environmental Science*, 2011, **4**, 3243-3262.
8. C. Renjie, L. Rui, H. Yongxin, W. Feng and L. Li, *Advanced Science*, 2016, **3**, 1600051.
9. G. Hautier, A. Jain, T. Mueller, C. Moore, S. P. Ong and G. Ceder, *Chemistry of Materials*, 2013, **25**, 2064-2074.
10. C. Wang, M. Sawicki, S. Emani, C. Liu and L. L. Shaw, *Electrochimica Acta*, 2015, **161**, 322-328.
11. J. Liu, L. Yin, X.-Q. Yang and P. G. Khalifah, *Chemistry of Materials*, 2018, **30**, 4609-4616.
12. J. Ding, Y.-C. Lin, J. Liu, J. Rana, H. Zhang, H. Zhou, I.-H. Chu, K. M. Wiaderek, F. Omenya, N. A. Chernova, K. W. Chapman, L. F. J. Piper, S.-P. Ong and M. S. Whittingham, *Advanced Energy Materials*, 2018, **8**, 1800221.
13. X.-P. Gao and H.-X. Yang, *Energy & Environmental Science*, 2010, **3**, 174-189.
14. G. Hautier, A. Jain, S. P. Ong, B. Kang, C. Moore, R. Doe and G. Ceder, *Chemistry of Materials*, 2011, **23**, 3495-3508.
15. Y.-C. Lin, M. F. V. Hidalgo, I.-H. Chu, N. A. Chernova, M. S. Whittingham and S. P. Ong, *Journal of Materials Chemistry A*, 2017, **5**, 17421-17431.
16. Y.-C. Lin, B. Wen, K. M. Wiaderek, S. Sallis, H. Liu, S. H. Lapidus, O. J. Borkiewicz, N. F. Quackenbush, N. A. Chernova, K. Karki, F. Omenya, P. J. Chupas, L. F. J. Piper, M. S. Whittingham, K. W. Chapman and S. P. Ong, *Chemistry of Materials*, 2016, **28**, 1794-1805.
17. C. Siu, I. D. Seymour, S. Britto, H. Zhang, J. Rana, J. Feng, F. O. Omenya, H. Zhou, N. A. Chernova, G. Zhou, C. P. Grey, L. F. J. Piper and M. S. Whittingham, *Chemical Communications*, 2018, **54**, 7802-7805.

18. M. Bianchini, J. M. Ateba-Mba, P. Dagault, E. Bogdan, D. Carlier, E. Suard, C. Masquelier and L. Croguennec, *Journal of Materials Chemistry A*, 2014, **2**, 10182-10192.

19. K. L. Harrison, C. A. Bridges, C. U. Segre, C. D. Varnado, D. Applestone, C. W. Bielawski, M. P. Paranthaman and A. Manthiram, *Chemistry of Materials*, 2014, **26**, 3849-3861.

20. M. Francis V. Hidalgo, Y.-C. Lin, A. Grenier, D. Xiao, J. Rana, R. Tran, H. Xin, M. Zuba, J. Donohue, F. O. Omenya, I.-H. Chu, Z. Wang, X. Li, N. A. Chernova, K. W. Chapman, G. Zhou, L. Piper, S. P. Ong and M. S. Whittingham, *Journal of Materials Chemistry A*, 2019, **7**, 8423-8432.

21. Y.-C. Lin, M. F. V. Hidalgo, I.-H. Chu, N. A. Chernova, M. S. Whittingham and S. P. Ong, *Journal of Materials Chemistry A*, 2017, **5**, 17421-17431.

22. C. Ling, R. Zhang and F. Mizuno, *Journal of Materials Chemistry A*, 2014, **2**, 12330-12339.

23. M. M. Ren, Z. Zhou, L. W. Su and X. P. Gao, *Journal of Power Sources*, 2009, **189**, 786-789.

24. K. H. Lii, C. H. Li, C. Y. Cheng and S. L. Wang, *Journal of Solid State Chemistry*, 1991, **95**, 352-359.

25. R. Gopal and C. Calvo, *Journal of Solid State Chemistry*, 1972, **5**, 432-435.

26. J.-M. Ateba Mba, C. Masquelier, E. Suard and L. Croguennec, *Chemistry of Materials*, 2012, **24**, 1223-1234.

27. Y. Song, P. Y. Zavalij and M. S. Whittingham, *Journal of The Electrochemical Society*, 2005, **152**, A721-A728.

28. H. Zhou, Y. Shi, F. Xin, F. Omenya and M. S. Whittingham, *ACS Applied Materials & Interfaces*, 2017, **9**, 28537-28541.

29. Y. Shi, H. Zhou, I. D. Seymour, S. Britto, J. Rana, L. W. Wangoh, Y. Huang, Q. Yin, P. J. Reeves, M. Zuba, Y. Chung, F. Omenya, N. A. Chernova, G. Zhou, L. F. J. Piper, C. P. Grey and M. S. Whittingham, *ACS Omega*, 2018, **3**, 7310-7323.

30. J. Rana, Y. Shi, M. J. Zuba, K. M. Wiaderek, J. Feng, H. Zhou, J. Ding, T. Wu, G. Cibin, M. Balasubramanian, F. Omenya, N. A. Chernova, K. W. Chapman, M. S. Whittingham and L. F. J. Piper, *Journal of Materials Chemistry A*, 2018, **6**, 20669-20677.

31. Y. Shi, H. Zhou, S. Britto, I. D. Seymour, K. M. Wiaderek, F. Omenya, N. A. Chernova, K. W. Chapman, C. P. Grey and M. S. Whittingham, *Electrochemistry Communications*, 2019, **105**, 106491.

32. F. Omenya, N. A. Chernova, Q. Wang, R. Zhang and M. S. Whittingham, *Chemistry of Materials*, 2013, **25**, 2691-2699.

33. F. Omenya, N. A. Chernova, S. Upreti, P. Y. Zavalij, K.-W. Nam, X.-Q. Yang and M. S. Whittingham, *Chemistry of Materials*, 2011, **23**, 4733-4740.

34. Z. Li, N. A. Chernova, J. Feng, S. Upreti, F. Omenya and M. S. Whittingham, *Journal of The Electrochemical Society*, 2011, **159**, A116-A120.

35. S. H. Kang and K. Amine, *Journal of Power Sources*, 2005, **146**, 654-657.

36. S.-W. Oh, S.-H. Park, J.-H. Kim, Y. C. Bae and Y.-K. Sun, *Journal of Power Sources*, 2006, **157**, 464-470.

37. H. J. Bang, V. S. Donepudi and J. Prakash, *Electrochimica Acta*, 2002, **48**, 443-451.

38. B. Wen, Q. Wang, Y. Lin, N. A. Chernova, K. Karki, Y. Chung, F. Omenya, S. Sallis, L. F. J. Piper, S. P. Ong and M. S. Whittingham, *Chemistry of Materials*, 2016, **28**, 3159-3170.

39. M. A. Bustam, Z. Man, S. Maitra and T. Ishihara, *Transactions of the Indian Ceramic Society*, 2013, **72**, 108-112.

40. S.-H. Lee and K.-S. Ryu, *Bulletin of the Korean Chemical Society*, 2018, **39**, 1266-1272.

41. D.-J. Park, R. Rajagopal and K.-S. Ryu, *Journal of Industrial and Engineering Chemistry*, 2020, **83**, 260-270.

42. S. Patoux and C. Masquelier, *Chemistry of Materials*, 2002, **14**, 5057-5068.

43. H. Morimoto, D. Ito, Y. Ogata, T. Suzuki, K. Sakamaki, T. Tsuji, M. Hirukawa, A. Matsumoto and S.-i. Tobishima, *Electrochemistry*, 2016, **84**, 878-881.

44. R. Du, Y. Bi, W. Yang, Z. Peng, M. Liu, Y. Liu, B. Wu, B. Yang, F. Ding and D. Wang, *Ceramics International*, 2015, **41**, 7133-7139.

45. I. M. Markus, F. Lin, K. C. Kam, M. Asta and M. M. Doeff, *The Journal of Physical Chemistry Letters*, 2014, **5**, 3649-3655.

46. H. Yang, C.-K. Lan and J.-G. Duh, *Journal of Power Sources*, 2015, **288**, 401-408.

47. F. Xin, H. Zhou, X. Chen, M. Zuba, N. Chernova, G. Zhou and M. Whittingham, *ACS Applied Materials & Interfaces*, 2019, **11**.

48. L. Ming, B. Zhang, Y. Cao, J.-F. Zhang, C.-H. Wang, X.-W. Wang and H. Li, *Frontiers in Chemistry*, 2018, **6**.

49. C. Kaplan, M. F. V. Hidalgo, M. J. Zuba, N. A. Chernova, L. F. J. Piper and M. S. Whittingham, *Journal of Materials Chemistry A*, 2021, **9**, 6933-6944.

50. K. Lee, C. Siu, M. F. V. Hidalgo, J. Rana, M. Zuba, Y. Chung, F. Omenya, L. F. J. Piper, H. Liu, N. A. Chernova and M. S. Whittingham, *ACS Applied Energy Materials*, 2021, **4**, 1421-1430.

51. C. Siu, M. J. Zuba, Y. Zong, H. Zhou, N. A. Chernova, L. F. J. Piper, G. Zhou and M. S. Whittingham, *Journal of The Electrochemical Society*, 2021, **168**, 060519.

52. B. H. Toby and R. B. Von Dreele, *Journal of Applied Crystallography*, 2013, **46**, 544-549.

53. P. J. Chupas, K. W. Chapman, C. Kurtz, J. C. Hanson, P. L. Lee and C. P. Grey, *Journal of Applied Crystallography*, 2008, **41**, 822-824.

54. D. O'Nolan, G. Huang, G. E. Kamm, A. Grenier, C.-H. Liu, P. K. Todd, A. Wustrow, G. Thinh Tran, D. Montiel, J. R. Neilson, S. J. L. Billinge, P. J. Chupas, K. S. Thornton and K. W. Chapman, *Journal of Applied Crystallography*, 2020, **53**, 662-670.

55. A. Drews, *Advances in X-Ray Analysis*, 2001, **44**.

56. H. Watanabe, N. Yamada and M. Okaji, *International Journal of Thermophysics*, 2004, **25**, 221-236.

57. V. Y. Bodryakov and A. A. Bykov, *Glass and Ceramics*, 2015, **72**, 67-70.

58. C. Ho, I. D. Raistrick and R. A. Huggins, *Journal of The Electrochemical Society*, 1980, **127**, 343.

59. A. Jain, S. P. Ong, G. Hautier, W. Chen, W. D. Richards, S. Dacek, S. Cholia, D. Gunter, D. Skinner, G. Ceder and K. A. Persson, *APL Materials*, 2013, **1**, 011002.

60. G. Kresse and J. Furthmüller, *Physical Review B*, 1996, **54**, 11169-11186.

61. P. E. Blöchl, *Physical Review B*, 1994, **50**, 17953-17979.

62. J. P. Perdew, K. Burke and M. Ernzerhof, *Physical Review Letters*, 1996, **77**, 3865-3868.

63. S. L. Dudarev, G. A. Botton, S. Y. Savrasov, C. J. Humphreys and A. P. Sutton, *Physical Review B*, 1998, **57**, 1505-1509.

64. S. P. Ong, S. Cholia, A. Jain, M. Brafman, D. Gunter, G. Ceder and K. A. Persson, *Computational Materials Science*, 2015, **97**, 209-215.
65. S.-H. Wei and S. B. Zhang, *Physical Review B*, 2002, **66**, 155211.
66. A. Togo and I. Tanaka, *Scripta Materialia*, 2015, **108**, 1-5.
67. P. J. Bleith, DOI: 10.3929/ethz-a-010342878, Dipl.-Ing., Technical University of Darmstadt 2014.
68. P. Bleith, M. Valla, P. Novák and C. Villevieille, *Journal of Materials Chemistry A*, 2014, **2**, 12513-12518.
69. K. Beneke and G. Lagaly, *Inorganic Chemistry*, 1983, **22**, 1503-1507.
70. K. Jacob, S. Raj and L. Rannesh, *International Journal of Materials Research*, 2007, **98**.
71. R. D. Shannon, *Acta Crystallographica Section A*, 1976, **32**, 751-767.
72. Z. W. Lebens-Higgins, D. M. Halat, N. V. Faenza, M. J. Wahila, M. Mascheck, T. Wiell, S. K. Eriksson, P. Palmgren, J. Rodriguez, F. Badway, N. Pereira, G. G. Amatucci, T.-L. Lee, C. P. Grey and L. F. J. Piper, *Scientific Reports*, 2019, **9**, 17720.